

FEDERAL UNIVERSITY OF ABC  
UNDERGRADUATE COURSE IN AEROESPACIAL ENGINEERING

Allan Moreira de Carvalho

REDUCED ORDER MODELS FOR DATA-DRIVEN NOZZLE FLOW FIELD  
RECONSTRUCTION USING MACHINE LEARNING

Santo André, SP – Brazil  
August 2025

Allan Moreira de Carvalho

REDUCED ORDER MODELS FOR DATA-DRIVEN NOZZLE FLOW FIELD  
RECONSTRUCTION USING MACHINE LEARNING

Monography presented to the Undergraduate course of Federal University of ABC, as a partial requirement for obtaining a Bachelor's degree in Aeroespacial Engineering.

Advisor: Prof. Dr. Wallace Gusmão Ferreira

Santo André, SP – Brazil  
August 2025

Allan Moreira de Carvalho,

Reduced Order Models for Data-Driven Nozzle Flow Field Reconstruction  
using Machine Learning/ Allan Moreira de Carvalho. – 2025.

54 p.: il.

Advisor: Prof. Dr. Wallace Gusmão Ferreira

Monography (BACHELOR) – Federal University of ABC, Undergraduate  
Course in Aeroespacial Engineering, Santo André, 2025.

1. Reduced Order Model. 2. Data-Driven. 3. Machine Learning. 4.  
Fluid Flow Reconstruction. I. Gusmão Ferreira, Wallace II. Undergraduate  
Course in Aeroespacial Engineering, 2025. III. Título.

This exemplar was revised and altered from the original version according to the observations done by the defense board at the defense day, under responsibility of author and advisor's consent.

Santo André, \_\_\_\_\_, 20 \_\_\_\_

Author's signature: \_\_\_\_\_

Advisor's signature: \_\_\_\_\_

---

SIGN SHEET

---

Signatures of examining board members, which examined and approved the defense of Monography of bachelor candidate Allan Moreira de Carvalho in August 15<sup>th</sup>, 2025:

---

- External Examiner

---

- Internal Substitute Examiner

---

- Chair

To my familia, for their constant support and encouragement, and to my mentors, for their invaluable guidance and inspiration.

## **Acknowledgement**

I would like to express my deepest gratitude to my advisor, Prof. Dr. Wallace Gusmão Ferreira, for his invaluable guidance, support, and encouragement throughout this journey. I am also profoundly thankful to my family and friends for their belief in me and their constant support. Finally, I extend my appreciation to my colleagues and collaborators who contributed to this work and made this experience truly enriching.

## **Epigraph**

*"The essence of knowledge is, having it, to apply it; not having it, to confess your ignorance."*

**Confucius**

## Abstract

The aerothermodynamic design of high-performance propulsion systems, such as rocket nozzles, presents a critical computational challenge. High-fidelity (HF) simulations, typically based on Reynolds-Averaged Navier-Stokes (RANS) equations coupled with conjugate heat transfer (CHT) models, provide the accurate wall heat flux predictions but are prohibitively expensive for multi-query applications, like design optimization and uncertainty quantification (UQ). On the other hand, low-fidelity (LF) models, such as quasi-one-dimensional Euler solvers, are computationally cheap but are unable to predict critical viscous and thermal phenomena. This dissertation addresses this dilemma by developing and validating a data-driven, multi-fidelity framework for the fast and accurate reconstruction of two-dimensional compressible and viscous flow fields in a water-cooled, convergent-divergent nozzle. The methodology uses a small database of paired LF and high fidelity HF simulations to train a computationally inexpensive surrogate model. Proper Orthogonal Decomposition (POD) is employed for dimensionality reduction, demonstrating exceptional efficiency by compressing the high-dimensional flow state into a latent space of just 3 principal components with negligible information loss. The central contribution of this work is the comparison of two surrogate modeling techniques for mapping the LF latent space to the HF latent space: the Artificial Neural Network (ANN) and a the Kriging interpolator. The results demonstrate the framework's success, with the Kriging-based Reduced Order Model (ROM) achieving a computational speedup of over 38,000 times compared to the HF simulation while maintaining remarkable accuracy, evidenced by a normalized root mean squared error of just 0.01% for the temperature field and 0.04% for the wall heat flux. A key finding is the superior performance of the Kriging model over the ANN, in this specific scenario, highlighting that for engineering problems characterized by smooth, low-dimensional mappings and limited data, traditional statistical methods can offer greater accuracy and efficiency, even beating recent machine learning architectures. This work provides a robust framework that breaks the trade-off between computational cost and accuracy, enabling previously intractable multi-query analyses essential for aerospace engineering.

**Keywords:** Reduced Order Model; Data-Driven; Machine Learning; Fluid Flow Reconstruction

## Resumo

O projeto aerotermodinâmico de sistemas de propulsão, como bocais de foguete, apresenta um desafio computacional crítico. Simulações de alta fidelidade (HF), tipicamente baseadas nas equações de Reynolds-Averaged Navier-Stokes (RANS) acopladas a modelos de transferência de calor conjugado (CHT), fornecem previsões precisas do fluxo de calor na parede, mas são proibitivamente caras para aplicações envolvendo múltiplas consultas, como otimização e quantificação de incerteza (UQ). Por outro lado, modelos de baixa fidelidade (LF), como as equações de Euler quase unidimensionais, são computacionalmente baratos, mas incapazes de prever fenômenos viscosos e térmicos. Esta dissertação aborda esse dilema ao desenvolver e validar uma estrutura (framework) multi-fidelidade orientada a dados para a reconstrução rápida e precisa de campos de escoamento bidimensionais, compressíveis e viscosos em um bocal convergente-divergente refrigerado a água. A metodologia utiliza um pequeno banco de dados pareado de simulações de baixa (LF) e alta fidelidade (HF) para treinar um modelo substituto (surrogate) de baixo custo computacional. A Decomposição Ortogonal Própria (POD) é empregada para a redução de dimensionalidade, demonstrando eficiência excepcional ao comprimir o estado de escoamento de alta dimensão em um espaço latente de apenas 3 componentes principais com perda de informação desprezível. A contribuição central deste trabalho é a comparação de duas técnicas de modelagem substituta para mapear o espaço latente de baixa fidelidade (LF) para o espaço latente de alta fidelidade (HF): a Rede Neural Artificial (ANN) e o interpolador Kriging. Os resultados demonstram o sucesso da estrutura, com o Modelo de Ordem Reduzida (ROM) baseado em Kriging alcançando uma aceleração computacional de mais de 38.000 vezes em comparação com a simulação de alta fidelidade, mantendo uma precisão notável, evidenciada por um erro médio quadrático normalizado (NRMSE) de apenas 0,01 % para o campo de temperatura e 0,04 % para o fluxo de calor na parede. Um achado fundamental é o desempenho superior do modelo de Kriging em relação à RNA, nesse cenário específico, destacando que para problemas de engenharia caracterizados por mapeamentos suaves, de baixa dimensão e com dados limitados, métodos estatísticos tradicionais podem oferecer grande precisão e eficiência, até mesmo superando recentes arquiteturas de aprendizado de máquina. Este trabalho fornece uma estrutura robusta que quebra o compromisso entre custo computacional e precisão, permitindo análises de múltiplas consultas antes intratáveis, essenciais para a engenharia aeroespacial.

**Palavras-chave:** Modelo de Ordem Reduzida; Baseado em Dados; Aprendizagem de Máquina; Reconstrução de Escoamentos de Fluidos

## List of Figures

Figure 1.1 Schematic representation of a convergent-divergent (De Laval) nozzle. The top panel shows the physical contour, identifying the subsonic converging section, the throat where the flow becomes sonic ( $M = 1$ ), and the supersonic diverging section. . . . .	20
Figure 1.2 Illustration of the qualitative behavior of key flow properties along the nozzle axis: pressure ( $p$ ) and temperature ( $T$ ) decrease, while Mach number ( $M$ ) increase. . . . .	21
Figure 1.3 Conceptual diagram of the conjugate heat transfer (CHT) problem in a cooled nozzle wall. The figure shows the coupled physics: convective heat transfer ( $q$ ) from the hot gas flow to the inner wall surface. . . . .	22
Figure 1.4 The data-driven ML-ROM methodology is divided into two stages. (a) The offline training stage is computationally expensive but performed only once. It involves generating paired high-fidelity (HF) and low-fidelity (LF) simulation snapshots, using Proper Orthogonal Decomposition (POD) to find low-dimensional bases, and training a surrogate model to map the LF coefficients to the HF coefficients. (b) The online prediction stage is computationally cheap and performed during inference on unseen parameters. It involves running a new fast LF simulation, projecting its result onto the LF basis, using the trained surrogate to predict the HF coefficients, and reconstructing the full HF flow field. . . . .	23
Figure 3.1 Verification of the low-fidelity (LF) quasi-1D Euler solver. Comparison of the in-house solver's predictions against reference numerical data from (Arina, 2004) for a standard nozzle test case with a shock wave. (a) Pressure profile. (b) Density profile. The excellent agreement, including the shock position and strength, verifies the correctness of the LF model implementation. . . . .	31
Figure 3.2 Computational domains used in the grid independence study. The figure shows the three grids with increasing refinement, highlighting the near-wall region resolution. . . . .	33

Figure 3.3 Comparison of high-fidelity SU2 simulation results with experimental data from (Back et al., 1964) for test case no. 313. (a) Centerline pressure distribution. (b) Wall temperature distribution. . . . .	35
Figure 4.1 Efficacy of Proper Orthogonal Decomposition (POD). (a) Normalized energy spectrum, showing the rapid decay of singular values, which indicates that the first few modes capture most of the system's energy. (b) Visualization of the first three dominant spatial POD modes for the temperature field, representing the fundamental patterns of temperature variation across the dataset. . . . .	39
Figure 4.2 Artificial Neural Network (ANN) model architecture. Schematic of the Multilayer Perceptron (MLP) used, showing the input layer (3 LF coefficients), ten hidden layers, and the output layer (3 HF coefficients). . . . .	41
Figure 4.3 Learning curve from the ANN training process. Mean Squared Error (MSE) versus training epochs for both the training and validation datasets. The convergence of both curves indicates successful training. . . . .	41
Figure 5.1 Temperature field: (a) ground truth (FOM), (b) ANN-ROM prediction, (c) absolute error. . . . .	44
Figure 5.2 Pressure field: (a) ground truth (FOM), (b) ANN-ROM prediction, (c) absolute error. . . . .	44
Figure 5.3 Mach number field: (a) ground truth (FOM), (b) ANN-ROM prediction, (c) absolute error. . . . .	44
Figure 5.4 Comparison of wall heat flux between the FOM and ANN-ROM. . . .	44
Figure 5.5 Temperature field: (a) ground truth (FOM), (b) Kriging-ROM prediction, (c) absolute error. . . . .	45
Figure 5.6 Pressure field: (a) ground truth (FOM), (b) Kriging-ROM prediction, (c) absolute error. . . . .	45
Figure 5.7 Mach number field: (a) ground truth (FOM), (b) Kriging-ROM prediction, (c) absolute error. . . . .	45
Figure 5.8 Comparison of wall heat flux between the FOM and Kriging-ROM. . . .	46

## List of Tables

Table 3.1 Numerical domains for the grid independence study. The table details the number of nodes in the axial ( $N_x$ ) and radial ( $N_y$ ) directions, the total number of cells ( $N_{cells}$ ), the grid refinement ratio ( $r$ ), and the approximate near-wall grid spacing in wall units ( $Y^+$ ) (Carvalho et al., 2023). . . . .	32
Table 3.2 Results for the grid independence study for average heat flux ( $q$ ), pressure ( $p$ ), and wall temperature ( $T$ ). The analysis confirms asymptotic convergence, justifying the selection of Grid 2 (Carvalho et al., 2023). . . . .	34
Table 3.3 Summary of the dataset generation and partitioning for machine learning model development. . . . .	36
Table 5.1 Computational cost and accuracy comparison for Kriging and Neural Network (NN) metamodels. Best results are in <b>bold</b> and worst results in <i>italics</i> . . . . .	46

## List of Abbreviations

- ANN Artificial Neural Network  
CFD Computational Fluid Dynamics  
CFL Courant-Friedrichs-Lowy  
CHT Conjugate Heat Transfer  
DMD Dynamic Mode Decomposition  
DNS Direct Numerical Simulation  
DoE Design of Experiments  
FOM Full-Order Model  
FVM Finite Volume Method  
GCI Grid Convergence Index  
HF High-Fidelity  
LF Low-Fidelity  
LHS Latin Hypercube Sampling  
ML Machine Learning  
MLP Multilayer Perceptron  
ML-ROM Machine Learning based Reduced Order Model  
MSE Mean Squared Error  
MUSCL Monotonic Upwind Scheme for Conservation Laws  
NRMSE Normalized Root Mean Squared Error  
NSGA-II Nondominated Sorting Genetic Algorithm II  
PCA Principal Component Analysis

POD Proper Orthogonal Decomposition

RANS Reynolds-Averaged Navier-Stokes

ROM Reduced Order Model

SST Shear Stress Transport

SVD Singular Value Decomposition

UQ Uncertainty Quantification

## List of Symbols

- $a_j$  Vetor de coeficientes do POD para o snapshot  $j$
- $\mathbf{a}_h, \mathbf{a}_l$  Vetores de coeficientes do POD de alta e baixa fidelidade
- $b_j$  Termo de bias do neurônio  $j$  na rede neural
- $c_{p,s}$  Capacidade de calor específica do sólido
- $d_h, d_l$  Dimensão do espaço latente de alta e baixa fidelidade
- $e$  Energia interna específica
- $E$  Energia total por unidade de massa
- $E_{tot}$  Energia total por unidade de volume
- $f$  Função de ativação da rede neural
- $f_{\text{surrogate}}$  Função do modelo substituto genérico
- $\mathbf{F}$  Vetor de fluxo das equações de Euler
- $\mathbf{F}^c, \mathbf{F}^v$  Vetores de fluxo convectivo e viscoso das equações de Navier-Stokes
- $\mathbf{I}$  Tensor identidade
- $k$  Condutividade térmica
- $\mathbf{K}$  Matriz de covariância do Kriging
- $\mathbf{k}_*$  Vetor de covariância do Kriging para um novo ponto
- $\mathcal{L}$  Função de custo (loss) da rede neural
- $m_h, m_l$  Dimensão (número de graus de liberdade) de um snapshot
- $M$  Número de Mach
- $n$  Número total de snapshots no dataset
- $N_{cells}$  Número total de células na malha

$N_{nodes}$  Número de nós na malha 2D

$N_{wall}$  Número de pontos na parede

$N_{1D}$  Número de pontos na malha 1D

$o_j$  Saída (output) do neurônio  $j$

$p$  Pressão estática

$p_{GCI}$  Ordem de convergência observada no estudo de malha

$q$  Fluxo de calor escalar ou médio

$\mathbf{q}$  Vetor de fluxo de calor no fluido

$\mathbf{q}_s$  Vetor de fluxo de calor difusivo no sólido

$\mathbf{Q}$  Vetor de termos-fonte das equações de Euler

$r$  Número de modos POD retidos na base truncada

$R$  Constante específica do gás

$\mathcal{R}$  Resíduo das equações de Navier-Stokes

$S$  Área da seção transversal do bocal

$t$  Tempo

$T$  Temperatura

$u$  Velocidade axial no escoamento 1D

$\mathbf{u}_i$  Vetor do  $i$ -ésimo modo espacial do POD

$\mathbf{U}$  Matriz de vetores singulares à esquerda (modos POD) do SVD

$U_s$  Variável conservada na equação de condução de calor

$\mathbf{v}$  Vetor de velocidade

$\mathbf{V}$  Matriz de vetores singulares à direita do SVD

$w_{ij}$  Peso da conexão entre os neurônios  $i$  e  $j$

$\mathbf{W}$  Vetor de variáveis conservadas (Euler e RANS)

$\mathbf{x}_h, \mathbf{x}_l$  Vetores de snapshot de alta e baixa fidelidade

- $\mathbf{X}_h, \mathbf{X}_l$  Matrizes de snapshot de alta e baixa fidelidade
- $\mathbf{y}$  Vetor de valores observados no treinamento do Kriging
- $Y^+$  Distância adimensional à parede
- $\gamma$  Razão entre os calores específicos
- $\mu$  Viscosidade dinâmica molecular
- $\mu_t$  Viscosidade turbulenta (de "eddy")
- $\mu_{\text{eff}}$  Viscosidade efetiva
- $\hat{\mu}$  Média estimada do processo Gaussiano (Kriging)
- $\rho$  Densidade
- $\rho_s$  Densidade do sólido
- $\sigma_i$  Valor singular  $i$  da matriz de snapshots
- $\Sigma$  Matriz diagonal de valores singulares
- $\boldsymbol{\tau}$  Tensor de tensões viscosas
- $\Psi_r$  Base de modos POD truncada com  $r$  modos
- $(\cdot)_0$  Condição de estagnação
- $(\cdot)_h$  Relativo à alta fidelidade (High-Fidelity)
- $(\cdot)_l$  Relativo à baixa fidelidade (Low-Fidelity)
- $(\cdot)_s$  Relativo ao domínio sólido (Solid)
- $(\cdot)_{in}$  Condição de entrada (Inlet)
- $(\cdot)_{exit}$  Condição de saída (Exit)
- $(\cdot)_j$  Índice do  $j$ -ésimo snapshot ou neurônio
- $(\cdot)_{i,j}$  Componente  $i, j$  de uma matriz ou tensor
- $(\cdot)^T$  Operador de transposição
- $(\cdot)^c$  Relativo ao fluxo convectivo
- $(\cdot)^v$  Relativo ao fluxo viscoso
- $(\hat{\cdot})$  Valor previsto ou estimado

# Contents

<b>1</b>	<b>Introduction</b>	<b>20</b>
1.1	The Convergent-Divergent Nozzle . . . . .	20
1.2	Physics of Convergent-Divergent Nozzle Flow . . . . .	20
1.3	Aerothermodynamic Design . . . . .	21
1.4	The Computational Bottleneck: Accuracy vs. Cost . . . . .	22
1.5	Multifidelity Surrogate Models . . . . .	23
1.6	Objectives and Contributions . . . . .	24
1.7	Dissertation Outline . . . . .	25
<b>2</b>	<b>Compressible Flow and Nozzle Aero thermodynamics</b>	<b>26</b>
2.1	Governing Equations of Fluid Dynamics . . . . .	26
2.1.1	The Euler Equations . . . . .	26
2.1.2	The Reynolds-Averaged Navier-Stokes (RANS) Equations . . . . .	26
2.2	Conjugate Heat Transfer and Solid Conduction . . . . .	28
<b>3</b>	<b>Computational Framework</b>	<b>30</b>
3.1	Low-Fidelity Simulation: The Quasi-1D Euler Solver . . . . .	30
3.1.1	Implementation and Numerical Method . . . . .	30
3.1.2	Numerical Verification . . . . .	30
3.2	High-Fidelity Simulation: The 2D RANS-CHT Approach . . . . .	31
3.2.1	The SU2 CFD Suite . . . . .	31
3.2.2	Model Setup . . . . .	31
3.2.3	Numerical Verification: Grid Independence Study . . . . .	32
3.2.4	Numerical Validation with Experimental Data . . . . .	34
3.3	Parametric Data Generation for Model Training . . . . .	35
<b>4</b>	<b>Data-Driven Flow Reconstruction via Reduced Order Modeling</b>	<b>37</b>
4.1	Reduced Order Modeling (ROM) . . . . .	37
4.2	Proper Orthogonal Decomposition (POD) . . . . .	37
4.2.1	The Snapshot Method . . . . .	38
4.2.2	Application and Efficacy . . . . .	38
4.3	Surrogate Modeling for Latent Space Mapping . . . . .	39

4.3.1	The Artificial Neural Network (ANN) Approximator . . . . .	40
4.3.2	The Kriging Interpolator . . . . .	41
<b>5</b>	<b>Analysis of Model Performance and Computational Efficiency</b>	<b>43</b>
5.1	Flow Field Reconstruction Accuracy . . . . .	43
5.1.1	Neural Network Reconstruction . . . . .	43
5.2	A Comparative Assessment of Surrogate Modeling Techniques . . . . .	46
5.3	Evaluation of Computational Gains and Engineering Impact . . . . .	47
<b>6</b>	<b>Synthesis, Conclusions, and Future Directions</b>	<b>48</b>
6.1	Synthesis of Findings . . . . .	48
6.2	Concluding Remarks . . . . .	48
6.3	Future Directions and Broader Impact . . . . .	49
	<b>Bibliography</b>	<b>51</b>

## Introduction

### 1.1 The Convergent-Divergent Nozzle

### 1.2 Physics of Convergent-Divergent Nozzle Flow

The convergent-divergent nozzle, often referred to as the De Laval nozzle, represents a fundamental technology in the field of high-speed aerospace propulsion (Anderson, 2003; Sutton; Biblarz, 2010). Its primary function is to accelerate a hot, high-pressure gas to supersonic velocities, generating thrust as a result. This is achieved by converting the thermal and pressure energy of the working fluid, typically the products of combustion, into kinetic energy (Sutton; Biblarz, 2010). The nozzle's characteristic shape is composed of a converging section, a minimum-area throat, and a diverging section, which is specifically designed to deal with the compressible transonic flow, as illustrated in Figure 1.1.

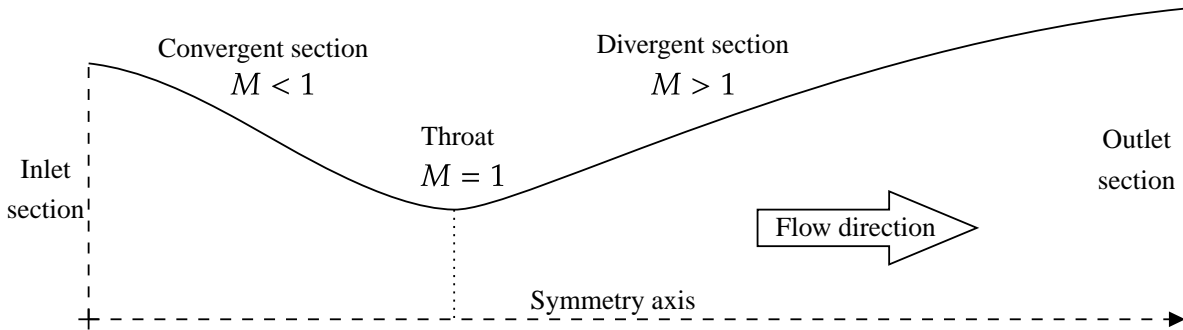


Figure 1.1: Schematic representation of a convergent-divergent (De Laval) nozzle. The top panel shows the physical contour, identifying the subsonic converging section, the throat where the flow becomes sonic ( $M = 1$ ), and the supersonic diverging section.

The operation of a De Laval nozzle is governed by the principles of isentropic compressible flow theory. As a pressurized gas enters the converging section at subsonic speed, its velocity increases while its pressure and temperature decrease. For a sufficiently low back pressure, the flow accelerates until it reaches sonic velocity (Mach = 1) precisely at the throat, the point of minimum cross-sectional area. This condition is known as choked flow (Sutton; Biblarz, 2010; White, 2011; Zucrow; Hoffman, 1976). Beyond the throat, in the diverging section, the flow continues to expand and accelerate into the supersonic regime. A graphical representation of these phenomena is provided in Figure 1.2. The thrust produced is determined by the momentum of the exiting gas and driven by the

pressure differential at the nozzle exit with respect to the inlet section, which shows up the critical importance of maximizing the exhaust velocity for efficient propulsion (Anderson, 2003).

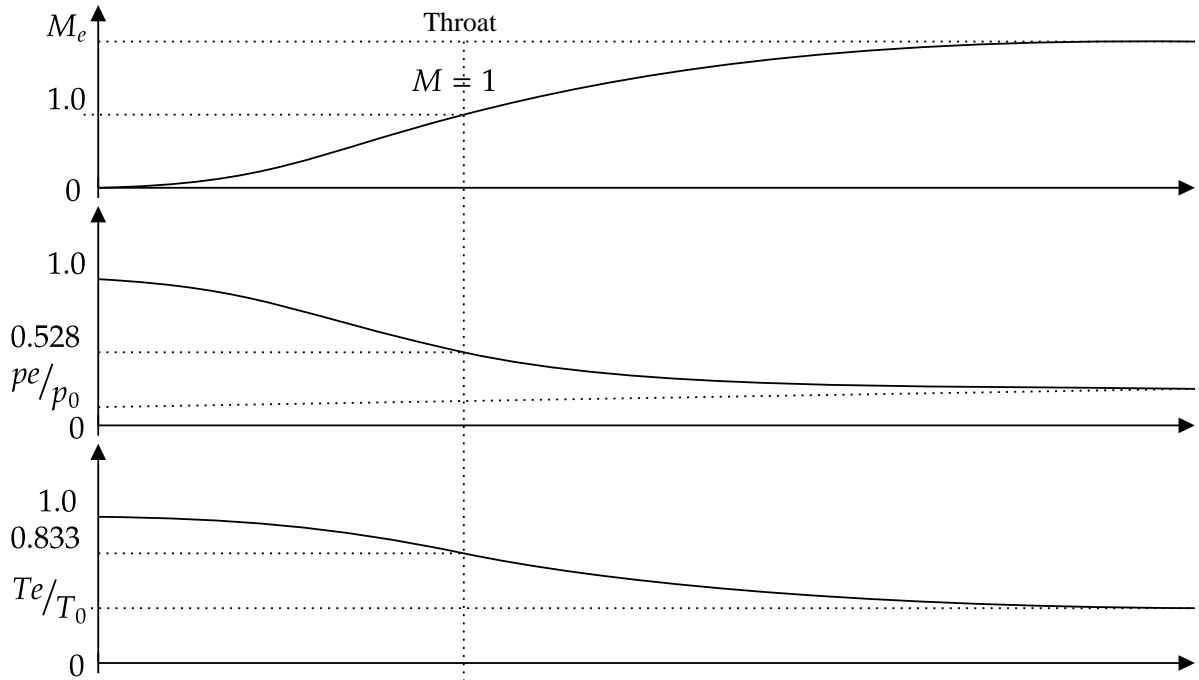


Figure 1.2: Illustration of the qualitative behavior of key flow properties along the nozzle axis: pressure ( $p$ ) and temperature ( $T$ ) decrease, while Mach number ( $M$ ) increase.

### 1.3 Aerothermodynamic Design

The operational condition within a convergent-divergent nozzle can become exceptionally severe, characterized by extreme temperatures and pressures that result in extreme thermomechanical stresses on the nozzle's wall structure (Back et al., 1964; Sutton; Biblarz, 2010). Consequently, a challenge in nozzle design is the management of heat transfer from the hot gas to the nozzle walls. This aerothermodynamic problem is critical to assure the structural integrity and operational reliability of the entire propulsion system . Uncontrolled wall temperatures can lead to material degradation, thermal fatigue, and catastrophic failure (Back et al., 1964).

To mitigate these risks, modern high-performance nozzles often incorporate active cooling systems, such as circulating water through channels within the nozzle walls. This makes the design problem into one of conjugate heat transfer (CHT), where the heat transfer within the fluid (convection) is intricately coupled with the heat transfer within the solid structure (conduction), as depicted in Figure 1.3. Accurately predicting the temperature distribution and heat flux at the fluid-solid interface is then not merely an academic exercise but a critical design requirement.

To simplify the complexity of coupled conjugate heat transfer problems, a common approach is to assume steady-state operation. This is a reasonable approximation for many practical applications where transient effects are negligible over the timescale of interest. Under this assumption, the fluid flow can be modeled using the steady-state Reynolds-Averaged Navier–Stokes (RANS) equations, along with appropriate turbulence models to account for the effects of turbulence on heat transfer. The heat transfer in the solid domain is typically modeled by the heat conduction equation, with boundary conditions defined by convective heat transfer from the fluid and any external cooling mechanisms. To further reduce computational cost, the coolant flow is not explicitly modeled. Instead, an average prescribed temperature can be imposed on the cooling surface of the outer nozzle wall, this simplifications are often acceptable for cases with high coolant flow rates (VALIDATION OF CONJUGATE HEAT-TRANSFER CAPABILITY FOR WATER-COOLED HIGH-SPEED FLOWS, ???).

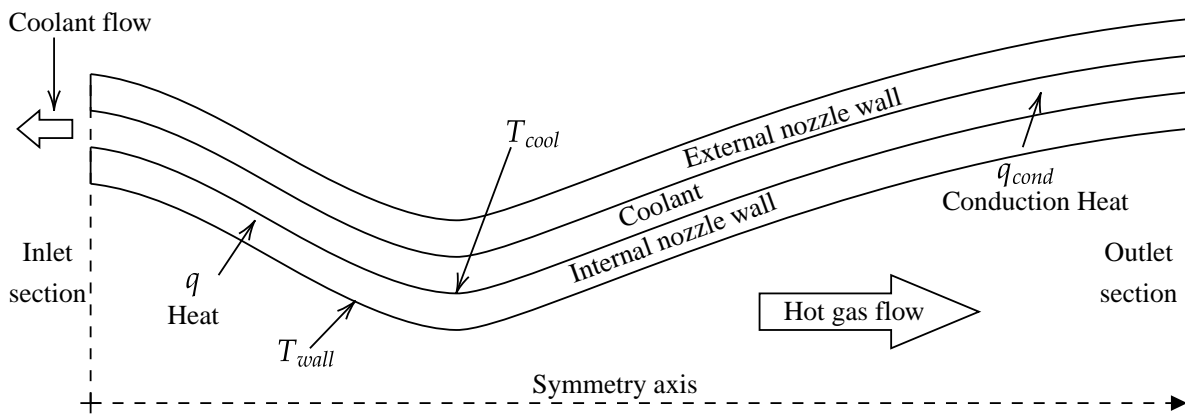


Figure 1.3: Conceptual diagram of the conjugate heat transfer (CHT) problem in a cooled nozzle wall. The figure shows the coupled physics: convective heat transfer ( $q$ ) from the hot gas flow to the inner wall surface.

## 1.4 The Computational Bottleneck: Accuracy vs. Cost

The modeling of such complex CHT phenomena necessitates the use of high-fidelity (HF) computational fluid dynamics (CFD) simulations, which typically solve the Reynolds-Averaged Navier-Stokes (RANS) equations. These simulations are capable of capturing the essential physics of turbulence, viscosity, and heat transfer that govern the system's behavior (Wilcox, 1998). However, the computational cost associated with these HF simulations can be huge, making them impractical for the mutli-query scenarios often faced in iterative engineering design cycles (Benner et al., 2015; Hesthaven et al., 2016,?; Quarteroni et al., 2016).

In contrast, low-fidelity (LF) models, such as simplified quasi-one-dimensional (quasi-1D) Euler solvers, are orders of magnitude faster. While these models can capture the

essential flow dynamics, like compressibility, their simplification assumptions, prevent them from predicting viscous effects such as boundary layer development and wall heat transfer (Carvalho et al., 2023). This creates a significant computational dilemma: the models that are fast enough are not accurate enough for the problem at hand, and the models that are accurate enough are far too slow for practical design cycles.

## 1.5 Multifidelity Surrogate Models

This work addresses the aforementioned computational dilemma by proposing a data-driven, multi-fidelity framework that combines the strengths of both HF and LF models. This approach is centered in the development of a Machine Learning based Reduced Order Model (ML-ROM), a computationally inexpensive surrogate that learns the relationship between the outputs of the HF and LF simulations (Benner et al., 2015; Carvalho et al., 2023; Hesthaven et al., 2016). This surrogate model acts like a sophisticated "black-box" approximator, trained on a pre-computed database of paired LF and HF solutions. The general workflow is depicted in Figure 1.4. Once trained, the ML-ROM can rapidly generate predictions with dimensionality of the HF model and competitive accuracy, but at a computational cost comparable, or even lower, than the LF model (Bekemeyer et al., 2025; Forrester et al., 2008; Yu; Hesthaven, 2019). This paradigm effectively breaks the trade-off between cost and accuracy, enabling the exploration of large design spaces.

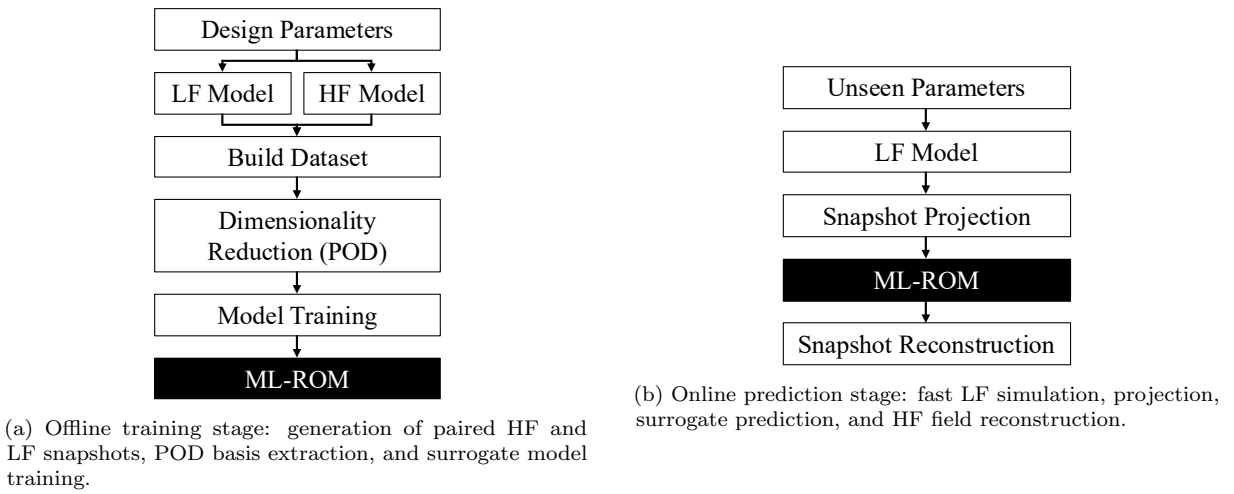


Figure 1.4: The data-driven ML-ROM methodology is divided into two stages. (a) The offline training stage is computationally expensive but performed only once. It involves generating paired high-fidelity (HF) and low-fidelity (LF) simulation snapshots, using Proper Orthogonal Decomposition (POD) to find low-dimensional bases, and training a surrogate model to map the LF coefficients to the HF coefficients. (b) The online prediction stage is computationally cheap and performed during inference on unseen parameters. It involves running a new fast LF simulation, projecting its result onto the LF basis, using the trained surrogate to predict the HF coefficients, and reconstructing the full HF flow field.

## 1.6 Objectives and Contributions

This work addresses the computational challenge in nozzle aerothermodynamic design by developing a multifidelity data-driven reduced-order model (ROM) able to account for viscous effects and recover 2D flow field solutions from simpler 1D inviscid model solutions. The dissertation was structured around the following key objectives:

- **Implement a multi-fidelity simulation environment:** To develop, verify, and validate both a high-fidelity RANS-CHT model and a computationally inexpensive quasi-1D Euler model to serve as the providers for the data-driven framework.
- **Apply dimensionality reduction to the flow sutions dataset:** To employ Proper Orthogonal Decomposition (POD) to compress the high-dimensional simulation data into a low-dimensional latent space, capturing the most energetic flow features with minimal data loss.
- **Compare surrogate modeling techniques:** To train and evaluate two different machine learning approaches: the Artificial Neural Network (ANN) and the Kriging interpolator, for the task of mapping between the low and high fidelity latent spaces.
- **Quantify the framework's performance:** To validate the end-to-end ML-ROM accuracy and computational efficiency on unseen test data.

The successful completion of these objectives resulted in the following scientific and technological contributions:

- **A Validated ML-ROM for Nozzle Aerothermodynamics:** The primary contribution is a complete, non-intrusive, data-driven framework capable of accurately reconstructing the 2D flow field and conjugate heat transfer in a cooled nozzle. This provides a practical tool for fast engineering design and optimization.
- **Insight on Surrogate Model Selection:** This work provides a finding for the engineering community: for simple problems with smooth, low-dimensional mappings and limited data, classical statistical methods like Kriging can be competitive and even greater than more complex machine learning architectures in both accuracy and efficiency.
- **Advancement in Computational Efficiency:** By achieving a computational speedup of over 38,000x with minimal loss of accuracy, the framework transforms previously intractable many-query analyses (e.g., design optimization, UQ) into feasible tasks.

## 1.7 Dissertation Outline

The subsequent chapters are structured as follows. Chapter 2 establishes the theoretical foundations of compressible flow, nozzle aerothermodynamics, and turbulence modeling. Chapter 2 details the multi-fidelity computational framework, including the setup, verification, and validation of the high and low-fidelity models. Chapter 3 presents the main data-driven methodology, explaining the principles of Reduced Order Modeling, Proper Orthogonal Decomposition, and the surrogate models employed. Chapter 5 provides an analysis of the framework's performance, comparing the accuracy and computational efficiency of the different approaches. Finally, Chapter 6 synthesizes the findings, draws conclusions, and outlines directions for future research.

## Compressible Flow and Nozzle Aerothermodynamics

### 2.1 Governing Equations of Fluid Dynamics

#### 2.1.1 The Euler Equations

The Euler equations form the mathematical basis for describing inviscid, compressible fluid flow. They represent the conservation of mass, momentum, and energy. For a quasi-one-dimensional flow through a duct with a varying cross-sectional area  $S(x)$ , these conservation laws can be expressed in the following conservative vector form, as presented in (Anderson, 2003):

$$\frac{\partial \mathbf{W}}{\partial t} + \frac{\partial \mathbf{F}}{\partial x} = \mathbf{Q} \quad (2.1)$$

, where  $\mathbf{W}$  is the vector of conserved variables,  $\mathbf{F}$  is the flux vector, and  $\mathbf{Q}$  is the source term vector. These vectors are defined as:

$$\mathbf{W} = \begin{pmatrix} \rho S \\ \rho u S \\ E_{tot} S \end{pmatrix}, \quad \mathbf{F} = \begin{pmatrix} \rho u S \\ (\rho u^2 + p)S \\ (E_{tot} + p)uS \end{pmatrix}, \quad \mathbf{Q} = \begin{pmatrix} 0 \\ p \frac{dS}{dx} \\ 0 \end{pmatrix} \quad (2.2)$$

In these expressions,  $\rho$  is the fluid density,  $u$  is the axial velocity,  $p$  is the static pressure, and  $E_{tot}$  is the total energy per unit volume, given by  $E_{tot} = \rho(e + u^2/2)$ , where  $e$  is the specific internal energy. For a calorically perfect gas, the system is closed using the ideal gas law,  $p = \rho RT$ , and the relation  $e = c_v T = p/((\gamma - 1)\rho)$ , where  $\gamma$  is the ratio of specific heats. The source term  $\mathbf{Q}$  arises from the dimensional reduction to a single spatial coordinate and accounts for the pressure forces exerted by the nozzle walls on the fluid as the area  $S(x)$  changes.

#### 2.1.2 The Reynolds-Averaged Navier-Stokes (RANS) Equations

The physical behavior of a viscous, heat-conducting, and compressible fluid is governed by the Navier-Stokes equations. These equations represent the conservation of mass, momentum, and energy, forming the complete mathematical description for the fluid dynamics simulations conducted in this work. For a comprehensive derivation of these fundamental principles from first principles, the reader is referred to foundational texts on the subject, such as the work by Versteeg and Malalasekera (Versteeg; Malalasekera, 2007).

In a conservative and differential form, as implemented within the SU2 software suite (SU2 Development Team, 2023), the compressible Navier-Stokes equations can be expressed compactly as:

$$\frac{\partial \mathbf{W}}{\partial t} + \nabla \cdot \mathbf{F}^c(\mathbf{W}) - \nabla \cdot \mathbf{F}^v(\mathbf{W}, \nabla \mathbf{W}) - \mathbf{S} = 0 \quad (2.3)$$

where  $\mathbf{W}$  is the vector of conserved variables,  $\mathbf{F}^c$  is the convective flux vector,  $\mathbf{F}^v$  is the viscous flux vector, and  $\mathbf{S}$  is a source term vector (assumed to be zero for this work). The vectors of conserved variables, convective fluxes, and viscous fluxes are defined, respectively, as:

$$\mathbf{W} = \begin{pmatrix} \rho \\ \rho\mathbf{v} \\ \rho E \end{pmatrix}, \quad \mathbf{F}^c = \begin{pmatrix} \rho\mathbf{v} \\ \rho\mathbf{v} \otimes \mathbf{v} + p\mathbf{I} \\ (\rho E + p)\mathbf{v} \end{pmatrix}, \quad \mathbf{F}^v = \begin{pmatrix} 0 \\ \boldsymbol{\tau} \\ \boldsymbol{\tau} \cdot \mathbf{v} + \mathbf{q} \end{pmatrix} \quad (2.4)$$

In these vectors,  $\rho$  is the fluid density,  $\mathbf{v}$  is the velocity vector,  $E$  is the total energy per unit mass,  $p$  is the static pressure, and  $\mathbf{I}$  is the identity tensor. The system is closed by the ideal gas law. The viscous stress tensor,  $\boldsymbol{\tau}$ , for a Newtonian fluid, and the heat flux vector,  $\mathbf{q}$ , based on Fourier's law of heat conduction, are given by:

$$\boldsymbol{\tau} = \mu (\nabla \mathbf{v} + (\nabla \mathbf{v})^T) - \frac{2}{3}\mu(\nabla \cdot \mathbf{v})\mathbf{I} \quad (2.5)$$

$$\mathbf{q} = k\nabla T \quad (2.6)$$

where  $\mu$  is the dynamic viscosity,  $k$  is the thermal conductivity, and  $T$  is the temperature.

While the Navier-Stokes equations provide a complete description of fluid motion, their direct numerical simulation (DNS) for the high-Reynolds-number turbulent flows characteristic of aerospace applications is computationally prohibitive. The vast range of turbulent length and time scales would require a grid resolution and time-step size that far exceed current computational capabilities for practical engineering problems. To overcome this limitation, a modeling approach is necessary. This work employs the Reynolds-Averaged Navier-Stokes (RANS) methodology, which involves time-averaging the instantaneous Navier-Stokes equations. This process decomposes flow variables into a mean component and a fluctuating component. The non-linearity of the convective term in the momentum equations gives rise to a new term, the Reynolds stress tensor  $(-\rho u'_i u'_j)$ , which represents the effect of turbulent fluctuations on the mean flow and creates a closure problem.

To close the system of RANS equations, the Reynolds stresses must be modeled. The Boussinesq hypothesis is invoked, which relates the Reynolds stresses to the mean rate of strain in a manner analogous to the relationship between viscous stresses and the strain rate in a Newtonian fluid. This is achieved by introducing a turbulent viscosity, or eddy viscosity ( $\mu_t$ ), which models the momentum transport caused by turbulent eddies.

Consequently, the effect of turbulence is accounted for by replacing the molecular dynamic viscosity ( $\mu$ ) with an effective viscosity ( $\mu_{\text{eff}} = \mu + \mu_t$ ). This allows the RANS equations to be solved in a form structurally identical to the original Navier-Stokes equations, with the turbulence model providing the value for  $\mu_t$ . In this study, the eddy viscosity is calculated using the two-equation Menter's Shear Stress Transport (SST)  $k-\omega$  model (Menter, 1994).

## 2.2 Conjugate Heat Transfer and Solid Conduction

The comprehensive aerothermodynamic analysis of a cooled structure, such as a rocket nozzle wall, is fundamentally a Conjugate Heat Transfer (CHT) problem. CHT analysis involves the simultaneous solution of heat transfer in distinct but thermally coupled physical domains: the fluid domain, governed by the RANS equations, and the solid domain, governed by the heat conduction equation.

Within the solid domain, the governing equation for heat transfer is the heat conduction equation. As implemented in the SU2 suite (SU2 Development Team, 2023), this equation is expressed in a general, differential form that can account for transient effects

$$\frac{\partial U_s}{\partial t} - \nabla \cdot \mathbf{F}^v(U_s, \nabla U_s) = 0 \quad (2.7)$$

where the conservative variable  $U_s$  and the diffusive flux vector  $\mathbf{F}^v$  are defined as:

$$U_s = \rho_s c_{p,s} T_s$$

$$\mathbf{F}^v(U_s, \nabla U_s) = k_s \nabla T_s$$

Here,  $T_s$  is the temperature field within the solid, while  $\rho_s$ ,  $c_{p,s}$ , and  $k_s$  are the density, specific heat capacity, and thermal conductivity of the solid material, respectively, which are assumed to be constant. For the steady-state problems considered in this work, the time-derivative term vanishes ( $\partial U_s / \partial t = 0$ ), and the governing equation simplifies to the well-known Laplace equation for heat conduction:

$$\nabla \cdot (k_s \nabla T_s) = 0 \quad (2.8)$$

This equation is solved numerically within the solid region by SU2's dedicated heat conduction solver. The solver discretizes the equation using a finite volume method (FVM) on a dual grid with vertex-based schemes, where the diffusive flux is evaluated at the midpoint of each control volume edge.

The critical aspect of a CHT simulation is the coupling at the fluid-solid interface. At this boundary, the physical conditions of temperature continuity and heat flux conservation must be enforced. Numerically, this is achieved through an iterative partitioned approach:

1. The RANS solver computes the flow field and determines the convective heat flux from the hot gas to the wall.
2. This heat flux is passed to the solid domain solver and applied as a boundary condition at the interface.
3. The heat conduction solver calculates the resulting temperature distribution throughout the solid wall.
4. The computed wall temperature at the interface is then passed back to the RANS solver as an updated thermal boundary condition for the fluid domain.

This iterative exchange of boundary data between the fluid and solid solvers continues until the temperature and heat flux values at the interface converge to a stable, self-consistent solution, accurately reflecting the coupled physics of the problem.

## Computational Framework

### 3.1 Low-Fidelity Simulation: The Quasi-1D Euler Solver

#### 3.1.1 Implementation and Numerical Method

The low-fidelity (LF) model is an in-house solver, developed in C++ leveraging the Eigen library for efficient array computations, and designed for maximum computational efficiency. The solver numerically integrates the quasi-1D Euler equations (Equation 2.1) on a structured, one-dimensional mesh to predict the core dynamics of the nozzle flow.

A Finite Volume Method is employed for the spatial discretization. To handle the convective terms, the Advection Upstream Splitting Method (AUSM) is used to compute the fluxes at the cell interfaces. This scheme is coupled with a second-order MUSCL (Monotonic Upwind Scheme for Conservation Laws) reconstruction to ensure sharp shock-capturing capabilities without introducing spurious numerical oscillations.

Time integration to a steady-state solution is performed using an explicit, fourth-order Runge-Kutta scheme. The stability of the time marching process is ensured by maintaining a constant Courant-Friedrichs-Lowy (CFL) number of 0.15. Furthermore, characteristic-based boundary conditions are implemented to correctly impose the stagnation properties at the inlet and the prescribed static pressure at the outlet (Hirsch, 1988, 1990).

#### 3.1.2 Numerical Verification

To verify the implemented LF model, its results were compared against published numerical data from a standard nozzle test case presented by Arina (2004). The geometry of the nozzle is defined by Equation 3.1 within the domain  $0 < x < L$ , with the throat located at  $x_t = 5.0$ .

$$S(x) = \begin{cases} 2.5 + 3 \left( \frac{x}{x_t} - 1.5 \right) \left( \frac{x}{x_t} \right)^2 & , \text{ if } x \leq x_t \\ 3.5 - \frac{x}{x_t} \left[ 6 - 4.5 \frac{x}{x_t} + \left( \frac{x}{x_t} \right)^2 \right] & , \text{ if } x > x_t \end{cases} \quad (3.1)$$

The input parameters for the simulation include a stagnation pressure of  $P_0 = 104,074$  kPa and a stagnation temperature of  $T_0 = 291.3$  K at the inlet. At the outlet, a static pressure of  $P_{\text{exit}} = 83,049$  kPa is prescribed. Air is modeled as an ideal gas with a specific gas constant  $R = 287$  J/kg · K and a ratio of specific heats  $\gamma = 1.4$ .

The comparison, shown in Figure 3.1, reveals excellent agreement between the in-house solver’s predictions and the reference data. Both the pressure and density profiles along the nozzle are accurately reproduced, including the precise capture of the shock wave’s position and strength. This verification confirms the LF model provides a reliable and accurate representation of the core, one-dimensional flow dynamics. The entire simulation for this verification case converges in under 2 seconds on a standard desktop CPU, validating its role as a computationally inexpensive model for the multi-fidelity framework.

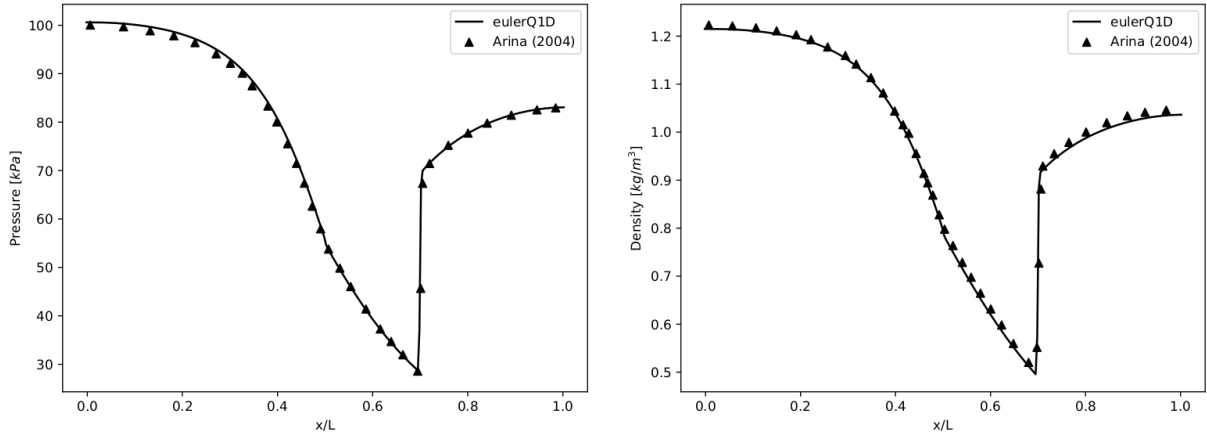


Figure 3.1: Verification of the low-fidelity (LF) quasi-1D Euler solver. Comparison of the in-house solver’s predictions against reference numerical data from (Arina, 2004) for a standard nozzle test case with a shock wave. (a) Pressure profile. (b) Density profile. The excellent agreement, including the shock position and strength, verifies the correctness of the LF model implementation.

## 3.2 High-Fidelity Simulation: The 2D RANS-CHT Approach

### 3.2.1 The SU2 CFD Suite

The high-fidelity simulations were conducted using the SU2 software suite, an open-source platform developed for multiphysics analysis and design optimization. SU2 (Stanford University Unstructured) is a collection of C++ and Python-based tools designed to solve partial differential equations on unstructured meshes using state-of-the-art numerical methods (Economou et al., 2016). Its robust capabilities for handling compressible flows, conjugate heat transfer, and a wide range of turbulence models make it a suitable choice for this research (Economou et al., 2016; Palacios et al., 2022).

### 3.2.2 Model Setup

The high-fidelity model was configured to solve the conjugate heat transfer problem in its entirety. Within the fluid domain, the Reynolds-Averaged Navier-Stokes (RANS) equations were solved using a finite volume method. The Menter’s SST turbulence model was employed to close the equations, as detailed in section 2.1.2. In the solid domain,

representing the nozzle wall, the energy equation was solved to model heat conduction. To achieve a steady-state solution, the simulation utilized an implicit Euler integration method coupled with time marching until convergence was reached at the fluid-solid interface.

The boundary conditions were specified to represent the nozzle's physical operation. At the fluid inlet, total pressure ( $p_{0in}$ ) and total temperature ( $T_{0in}$ ) were defined as stagnation properties. The outlet was defined with a static pressure condition ( $p_{exit}$ ). The nozzle's centerline was treated as a symmetry axis. A no-slip condition was applied at the inner nozzle wall, which also served as the coupled interface for the conjugate heat transfer (CHT) problem. On the outer surface of the solid wall, representing the cooling channel, a constant temperature of 300 K was imposed, a common simplification for high-efficiency cooling systems

### 3.2.3 Numerical Verification: Grid Independence Study

A critical step in any CFD analysis is verification, which ensures that the numerical solution is not an artifact of the computational grid. A grid independence study was performed using the Grid Convergence Index (GCI) method proposed by Roache (1994) to quantify the discretization error (Carvalho et al., 2023). Three structured grids of increasing refinement were generated, as detailed in Table 3.1.

Table 3.1: Numerical domains for the grid independence study. The table details the number of nodes in the axial ( $N_x$ ) and radial ( $N_y$ ) directions, the total number of cells ( $N_{cells}$ ), the grid refinement ratio ( $r$ ), and the approximate near-wall grid spacing in wall units ( $Y^+$ ) (Carvalho et al., 2023).

	$N_x$	$N_y$	$N_{cells}$	$r$	$Y^+$
<b>Grid 1</b>	270	440	118091	1.3	$\approx 1$
<b>Grid 2</b>	210	330	68761	1.3	$\approx 2$
<b>Grid 3</b>	160	250	39591		$\approx 3$

Figure 3.2 illustrates the computational domains selected by the GCI analysis. The grids were designed to ensure that the near-wall region was adequately resolved, with the wall spacing ( $Y^+$ ) kept below 3, which is generally acceptable for RANS simulations (Carvalho et al., 2023).

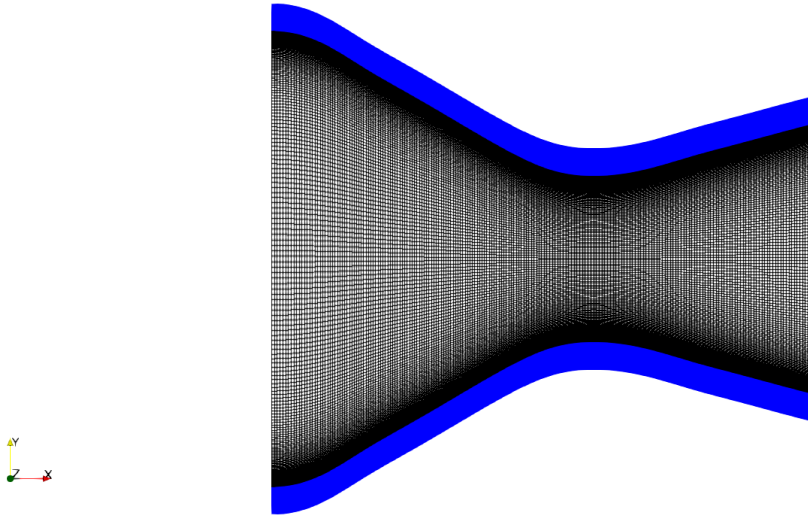


Figure 3.2: Computational domains used in the grid independence study. The figure shows the three grids with increasing refinement, highlighting the near-wall region resolution.

The GCI was calculated for key output quantities: average heat flux along the wall ( $q$ ), pressure along the centerline ( $p$ ), and temperature at the wall ( $T$ ). The results, summarized in Table 3.2, show that the solutions exhibit monotonic and asymptotic convergence, as indicated by the positive order of convergence ( $p_{GCI}$ ) and small GCI values. An asymptotic ratio ( $GCI_{asymptotic}$ ) close to 1 signifies that the solution is in the asymptotic range of convergence and is effectively grid-independent. Based on this rigorous analysis, Grid 2 was selected for all subsequent high-fidelity simulations, as it provided a reliable solution with a manageable cell count. This verification process is fundamental to the entire study, as it establishes a credible and converged high-fidelity baseline against which the reduced-order models are ultimately judged.

Table 3.2: Results for the grid independence study for average heat flux ( $q$ ), pressure ( $p$ ), and wall temperature ( $T$ ). The analysis confirms asymptotic convergence, justifying the selection of Grid 2 (Carvalho et al., 2023).

	$q$ [ $W/m^2$ ]	$N_{cells}$	$r$	GCI	$GCI_{asymptotic}$	$p_{GCI}$
<b>Grid 1</b>	$519 \times 10^3$	118091	1.3	6.95%		
<b>Grid 2</b>	$502 \times 10^3$	68761	1.3	11.40%	1.034	1.71
<b>Grid 3</b>	$475 \times 10^3$	39591				
	$p$ [kPa]	$N_{cells}$	$r$	GCI	$GCI_{asymptotic}$	$p_{GCI}$
<b>Grid 1</b>	$737 \times 10^3$	118091	1.3	0.23%		
<b>Grid 2</b>	$736 \times 10^3$	68761	1.3	0.30%	1.001	1.02
<b>Grid 3</b>	$736 \times 10^3$	39591				
	$T$ [K]	$N_{cells}$	$r$	GCI	$GCI_{asymptotic}$	$p_{GCI}$
<b>Grid 1</b>	518	118091	1.3	0.17%		
<b>Grid 2</b>	520	68761	1.3	0.47%	0.998	3.73
<b>Grid 3</b>	523	39591				

### 3.2.4 Numerical Validation with Experimental Data

Following verification, the high-fidelity model was validated by comparing its predictions against experimental data for test case no. 313 from (Back et al., 1964). This validation process faced certain challenges due to incomplete information in the reference study, such as the exact composition of the nozzle wall, which was assumed to be AISI 302 stainless steel. Furthermore, the boundary condition for the outer cooling wall was simplified to a constant temperature of 300 K. Despite these limitations, the validation showed promising results, as seen in Figure 3.3. The predicted pressure distribution along the nozzle centerline demonstrated good agreement with the experimental measurements. While the predicted wall temperature showed a slight deviation, likely attributable to the simplified boundary conditions and material property assumptions, the overall agreement was sufficient to establish confidence in the high-fidelity model's ability to capture the essential physics of the problem.

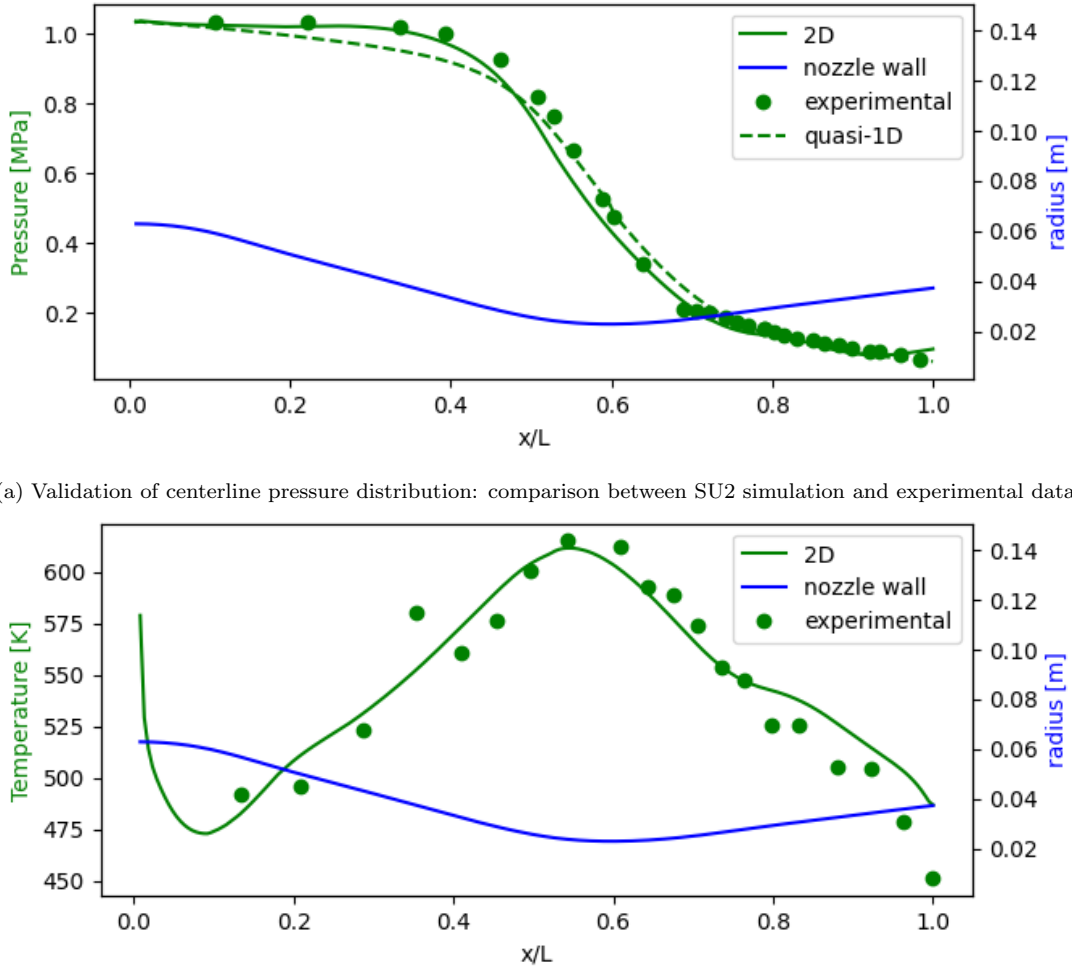


Figure 3.3: Comparison of high-fidelity SU2 simulation results with experimental data from (Back et al., 1964) for test case no. 313. (a) Centerline pressure distribution. (b) Wall temperature distribution.

### 3.3 Parametric Data Generation for Model Training

To train the data-driven surrogate models, a comprehensive dataset mapping the low-fidelity inputs to the high-fidelity outputs was required. This dataset was generated by running 181 paired simulations, where each pair consisted of one LF and one HF simulation for the same set of boundary conditions. The key parameter varied across these simulations was the inlet total temperature ( $T_{0in}$ ), which was sampled across a range of 285 K to 1115 K.

While the inlet total temperature was varied, other key boundary conditions were held constant across all 181 simulations to isolate its effect. Specifically, the inlet total pressure ( $P_{0in}$ ) was fixed at 1191.0 kPa and the outlet static pressure ( $P_{exit}$ ) was set to 101.0 kPa.

Each simulation result constitutes a "snapshot" of the flow field. Specifically, a high-fidelity (HF) snapshot is a single vector containing the complete 2D field data, while

a low-fidelity (LF) snapshot consists of the flattened 1D data from the Euler solver. The collection of these paired snapshots forms the final dataset used for the subsequent dimensionality reduction and model training stages.

For each simulation  $j$ , the high-fidelity snapshot vector  $\mathbf{x}_{h,j} \in \mathbb{R}^{m_h}$  is constructed by concatenating the flattened vectors of pressure ( $\mathbf{p}_h$ ), temperature ( $\mathbf{T}_h$ ), and Mach number ( $\mathbf{M}_h$ ) from all  $N_{nodes}$  grid points, along with the wall heat flux ( $\mathbf{q}_w$ ) at the  $N_{wall}$  wall points:

$$\mathbf{x}_{h,j} = \begin{bmatrix} \mathbf{p}_h \\ \mathbf{T}_h \\ \mathbf{M}_h \\ \mathbf{q}_w \end{bmatrix}_j, \quad \text{where } m_h = 3 \times N_{nodes} + N_{wall}. \quad (3.2)$$

Similarly, the corresponding low-fidelity snapshot vector  $\mathbf{x}_{l,j} \in \mathbb{R}^{m_l}$  is composed of the flattened 1D data for pressure ( $\mathbf{p}_l$ ), temperature ( $\mathbf{T}_l$ ), and Mach number ( $\mathbf{M}_l$ ) from the  $N_{1D}$  points of the Euler solver's mesh:

$$\mathbf{x}_{l,j} = \begin{bmatrix} \mathbf{p}_l \\ \mathbf{T}_l \\ \mathbf{M}_l \end{bmatrix}_j, \quad \text{where } m_l = 3 \times N_{1D}. \quad (3.3)$$

To ensure efficient and uniform exploration of this parameter space, Latin Hypercube Sampling (LHS) was employed. LHS is a statistical method for Design of Experiments (DoE) that generates a more representative sample of the parameter space compared to simple random sampling, making it a standard and effective practice for generating training data for surrogate models (Yu; Hesthaven, 2019). The resulting dataset of 181 snapshot pairs was then partitioned into three subsets for the machine learning workflow: 145 pairs for training the models, 18 for validation during the training process to prevent overfitting, and a final 18 pairs held out as a blind test set to evaluate the final performance of the trained models. A summary of the dataset is provided in Table 3.3.

Table 3.3: Summary of the dataset generation and partitioning for machine learning model development.

Purpose	# of Samples	Sampling Method	Parameter Varied	Range
Training	145	LHS	$T_{0in}$	285 K - 1115 K
Validation	18	LHS	$T_{0in}$	285 K - 1115 K
Testing	18	LHS	$T_{0in}$	285 K - 1115 K
<b>Total</b>	<b>181</b>			

## Data-Driven Flow Reconstruction via Reduced Order Modeling

### 4.1 Reduced Order Modeling (ROM)

Reduced Order Modeling is a paradigm designed to address the computational bottleneck inherent in high-fidelity simulations. ROMs create computationally inexpensive, low-dimensional surrogate models that approximate the behavior of a full-order, complex system (Brunton; Kutz, 2019; Stabile; Rozza, 2021). These models are particularly valuable in many-query contexts like optimization, control, and uncertainty quantification, where repeated evaluations of the full model are infeasible. ROMs can be broadly categorized into two classes: intrusive and non-intrusive. Intrusive methods, such as Galerkin projection, require modification of the governing equation solvers. In contrast, non-intrusive methods are purely data-driven, treating the full-order model as a black box and learning the input-output relationship from simulation data (Benner et al., 2015; Hesthaven et al., 2016). The framework developed in this dissertation falls into the non-intrusive category.

### 4.2 Proper Orthogonal Decomposition (POD)

A foundational step in building an effective ROM is dimensionality reduction. Proper Orthogonal Decomposition (POD) is a powerful mathematical technique for extracting a low-dimensional basis that optimally captures the variance within a high-dimensional dataset (Berkooz et al., 1993; Holmes et al., 2012; Sirovich, 1987). Mathematically, POD is equivalent to Principal Component Analysis (PCA) and is implemented via the Singular Value Decomposition (SVD) of the data matrix. The method decomposes a complex, spatiotemporal field into a set of orthogonal spatial modes (the POD modes) and corresponding temporal coefficients. These modes are hierarchical; the first mode captures the most energy (or variance) in the data, the second captures the most of the remaining energy, and so on. This property allows for an extremely efficient, low-rank approximation of the original data by retaining only the first few most energetic modes (Rowley; Dawson, 2017; Taira et al., 2017). The core of the method is the SVD of a snapshot matrix  $\mathbf{X}$ , which is detailed in the following section. A full mathematical formulation of POD is provided in Appendix B.

### 4.2.1 The Snapshot Method

The specific implementation of POD used in this study is the snapshot method. The process begins by assembling the individual snapshot vectors, which were defined in the previous chapter, into high-fidelity and low-fidelity snapshot matrices. Each of the  $n = 181$  snapshot vectors from the simulations becomes a column in its respective matrix,  $\mathbf{X}_h \in \mathbb{R}^{m_h \times n}$  and  $\mathbf{X}_l \in \mathbb{R}^{m_l \times n}$ . This column-wise assembly is represented as:

$$\mathbf{X}_h = \begin{bmatrix} | & | & & | \\ \mathbf{x}_{h,1} & \mathbf{x}_{h,2} & \dots & \mathbf{x}_{h,n} \\ | & | & & | \end{bmatrix}, \quad \mathbf{X}_l = \begin{bmatrix} | & | & & | \\ \mathbf{x}_{l,1} & \mathbf{x}_{l,2} & \dots & \mathbf{x}_{l,n} \\ | & | & & | \end{bmatrix} \quad (4.1)$$

where  $m_h$  and  $m_l$  are the total number of degrees of freedom for a single high- and low-fidelity snapshot, respectively. These matrices contain the complete dataset and serve as the direct input for the Singular Value Decomposition (SVD).

The SVD is then performed on these matrices. For a generic snapshot matrix  $\mathbf{X}$ , the SVD is given by:

$$\mathbf{X} = \mathbf{U}\Sigma\mathbf{V}^T \quad (4.2)$$

where  $\mathbf{U} \in \mathbb{R}^{m \times m}$  is an orthogonal matrix whose columns are the left singular vectors (the POD spatial modes),  $\Sigma \in \mathbb{R}^{m \times n}$  is a diagonal matrix of singular values  $\sigma_i$ , and  $\mathbf{V} \in \mathbb{R}^{n \times n}$  is an orthogonal matrix whose columns are the right singular vectors (related to the temporal coefficients).

By projecting the high-dimensional snapshot data onto a small number of these modes (a truncated basis  $\Psi_r = [\mathbf{u}_1, \dots, \mathbf{u}_r]$ ), one obtains a set of low-dimensional coefficients that serve as a compact representation of the full system state. The approximation of a snapshot  $\mathbf{x}_j$  and the calculation of its coefficient vector  $\mathbf{a}_j$  are given by:

$$\mathbf{x}_j \approx \Psi_r \mathbf{a}_j \quad (4.3)$$

$$\mathbf{a}_j = \Psi_r^T \mathbf{x}_j \quad (4.4)$$

### 4.2.2 Application and Efficacy

The application of POD to the nozzle flow dataset yielded a remarkable degree of dimensionality reduction. The high-fidelity state, originally described by 208,110 degrees of freedom (the number of grid points times the number of variables), was accurately represented using only 3 POD modes. The effectiveness of this compression is visualized in Figure 4.1. The energy spectrum shows a rapid decay, indicating that the vast majority of the system's variance is captured by the first few modes. The projection error associated with this truncation was exceptionally low, with an average global relative error in

the temperature field of just 0.0006% and a maximum error for a sample case of only 0.0133% (Carvalho et al., 2023). This demonstrates the extraordinary efficiency of POD in compressing the vast amount of information contained in the CFD solutions into a highly compact, latent variable representation with negligible loss of information.

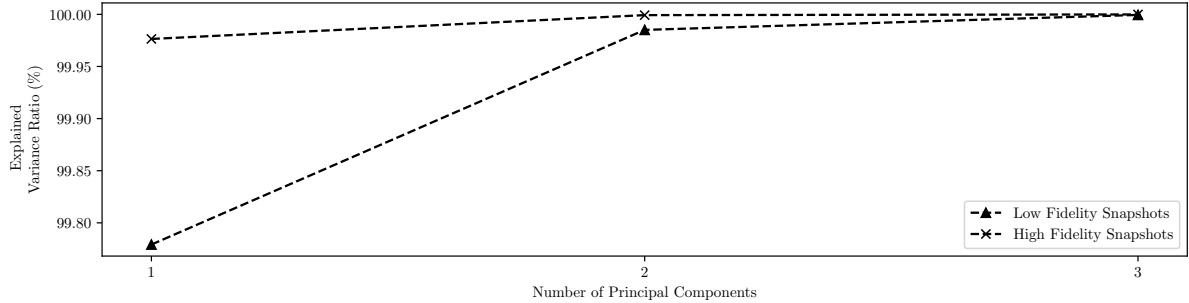


Figure 4.1: Efficacy of Proper Orthogonal Decomposition (POD). (a) Normalized energy spectrum, showing the rapid decay of singular values, which indicates that the first few modes capture most of the system’s energy. (b) Visualization of the first three dominant spatial POD modes for the temperature field, representing the fundamental patterns of temperature variation across the dataset.

This powerful compression is the key enabler for the entire surrogate modeling framework. The original problem—mapping a 633-dimensional low-fidelity state vector to a 208,110-dimensional high-fidelity state vector—is a high-dimensional regression task that would be intractable for any machine learning model without an enormous dataset. POD transforms this problem. It acts as an expert feature extractor, identifying the fundamental building blocks (the modes) of the flow. The complex task of learning the spatially distributed physics is thus converted into a much simpler one: learning the mapping between the 10 coefficients of the low-fidelity model and the 10 coefficients of the high-fidelity model. In this synergistic partnership, POD performs the heavy lifting of identifying the relevant physical structures, while the surrogate model learns the relatively simple correlation between their amplitudes. This synergy is the cornerstone of the framework’s success.

### 4.3 Surrogate Modeling for Latent Space Mapping

Once the dimensionality of the problem has been reduced via POD, a surrogate model is required to learn the nonlinear mapping from the low-fidelity latent space to the high-fidelity latent space. This study compares two distinct approaches for this task: an Artificial Neural Network and a Kriging interpolator.

The goal is to construct a function,  $f_{\text{surrogate}}$ , that approximates the relationship between the low-fidelity (LF) and high-fidelity (HF) POD coefficients. Given a training dataset of  $N_{\text{train}}$  paired coefficients,  $\{(\mathbf{a}_{l,j}, \mathbf{a}_{h,j})\}_{j=1}^{N_{\text{train}}}$ , the surrogate model aims to learn the mapping:

$$\mathbf{a}_h \approx \hat{\mathbf{a}}_h = f_{\text{surrogate}}(\mathbf{a}_l) \quad (4.5)$$

where  $\mathbf{a}_l \in \mathbb{R}^{d_l}$  is the vector of LF coefficients,  $\mathbf{a}_h \in \mathbb{R}^{d_h}$  is the vector of true HF coefficients, and  $\hat{\mathbf{a}}_h$  is the prediction from the surrogate model. This study compares two distinct approaches for this task: an Artificial Neural Network and a Kriging interpolator.

### 4.3.1 The Artificial Neural Network (ANN) Approximator

Artificial Neural Networks are powerful computational models inspired by biological neural systems, renowned for their ability to act as universal function approximators (Hornik et al., 1989). The specific architecture used here is a dense Multilayer Perceptron (MLP), which consists of an input layer, multiple hidden layers of interconnected "neurons," and an output layer. Each connection has an associated weight, and each neuron applies a nonlinear activation function to its input. The output  $o_j$  of a single neuron is calculated as:

$$o_j = f \left( \sum_i w_{ij} x_i + b_j \right) \quad (4.6)$$

where  $w_{ij}$  are the weights,  $x_i$  are the inputs from the previous layer,  $b_j$  is a bias term, and  $f$  is a nonlinear activation function. The network "learns" by adjusting these weights and biases through a process called back-propagation, which uses gradient descent to minimize a loss function (e.g., Mean Squared Error) between the network's predictions and the true data (Yu; Hesthaven, 2019).

The entire MLP represents a complex, nested function,  $f_{\text{ANN}}$ , parameterized by the set of all weights  $\mathbf{W}$  and biases  $\mathbf{b}$ . For a given input vector of LF coefficients  $\mathbf{a}_l$ , the network produces a prediction for the HF coefficients  $\hat{\mathbf{a}}_h$ :

$$\hat{\mathbf{a}}_h = f_{\text{ANN}}(\mathbf{a}_l; \mathbf{W}, \mathbf{b}) \quad (4.7)$$

The network "learns" by adjusting the parameters  $\mathbf{W}$  and  $\mathbf{b}$  through a process called back-propagation, which uses gradient descent to minimize a loss function. In this work, the Mean Squared Error (MSE) between the network's predictions and the true data is minimized:

$$\mathcal{L}(\mathbf{W}, \mathbf{b}) = \frac{1}{N_{\text{train}}} \sum_{j=1}^{N_{\text{train}}} \|\mathbf{a}_{h,j} - f_{\text{ANN}}(\mathbf{a}_{l,j}; \mathbf{W}, \mathbf{b})\|_2^2 \quad (4.8)$$

The implementation in this work utilized the TensorFlow library to construct a dense MLP with the architecture illustrated in Figure 4.2: an input layer with 3 neurons (for the 3 LF POD coefficients), 10 hidden layers each containing 10 neurons, and an output

layer with 3 neurons (for the 3 HF POD coefficients). The hyperbolic tangent ('tanh') was used as the activation function for the hidden layers, and the ADAM optimizer was employed for efficient training. The training history, shown in Figure 4.3, displays a rapid decrease in both the training and validation loss functions, indicating effective learning of the mapping between the latent spaces without significant overfitting.

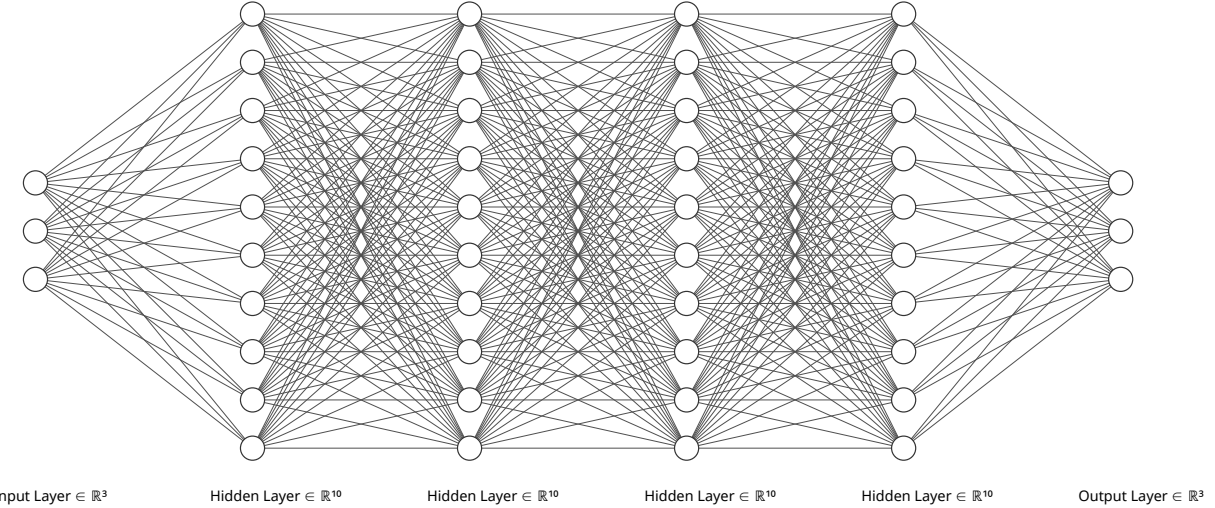


Figure 4.2: Artificial Neural Network (ANN) model architecture. Schematic of the Multilayer Perceptron (MLP) used, showing the input layer (3 LF coefficients), ten hidden layers, and the output layer (3 HF coefficients).

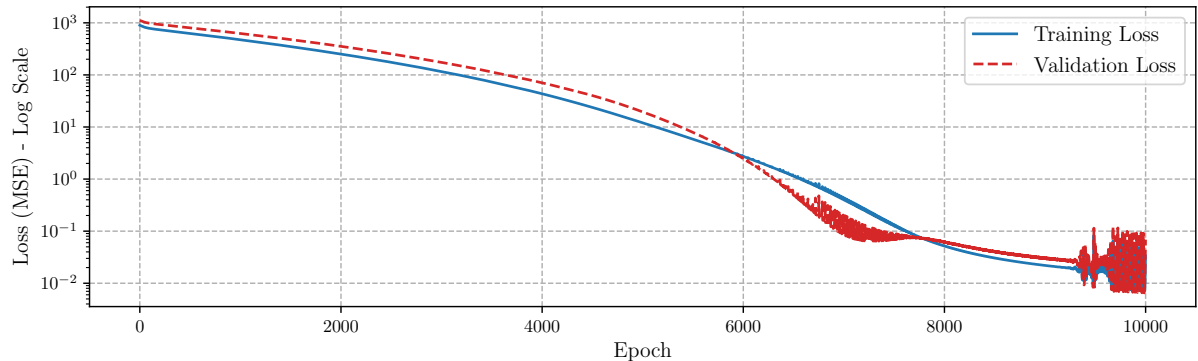


Figure 4.3: Learning curve from the ANN training process. Mean Squared Error (MSE) versus training epochs for both the training and validation datasets. The convergence of both curves indicates successful training.

### 4.3.2 The Kriging Interpolator

Kriging, also known as Gaussian Process Regression, is a sophisticated statistical interpolation method that has its roots in geostatistics (Rasmussen; Williams, 2006; Sacks et al., 1989). It frames the interpolation problem from a Bayesian perspective, modeling the unknown function as a realization of a Gaussian process. A prediction at a new point is calculated as a weighted average of the known training data points. Crucially, these weights are not based on simple distance but are determined by a statistical model of

spatial correlation (a covariance function or variogram) that is learned from the data itself (Jones et al., 1998; Ng; Hughes, 2018). The Ordinary Kriging predictor for a value at a new point  $x_*$  is given by:

$$\hat{f}(x_*) = \hat{\mu} + \mathbf{k}_*^T \mathbf{K}^{-1} (\mathbf{y} - \hat{\mu} \mathbf{1}) \quad (4.9)$$

where  $\hat{\mu}$  is the estimated mean,  $\mathbf{y}$  is the vector of observed training values,  $\mathbf{K}$  is the covariance matrix of the training points, and  $\mathbf{k}_*$  is the vector of covariances between the training points and the new point. A key advantage of Kriging is that, in addition to providing a prediction (the mean of the posterior distribution), it also provides a measure of the prediction uncertainty (the variance), which can be invaluable for engineering analysis.

Since standard Kriging is a single-output method, a multi-output prediction for the vector  $\hat{\mathbf{a}}_h = [\hat{a}_{h,1}, \dots, \hat{a}_{h,d_h}]^T$  is achieved by constructing an independent Kriging model,  $f_{\text{Kriging},i}$ , for each of the  $d_h$  components of the HF coefficient vector. Each model is trained on the full vector of LF coefficients  $\mathbf{a}_l$  to predict its corresponding scalar output component  $a_{h,i}$ :

$$\hat{a}_{h,i} = f_{\text{Kriging},i}(\mathbf{a}_l), \quad \text{for } i = 1, \dots, d_h \quad (4.10)$$

The implementation in this study employed ordinary Kriging with an exponential covariance model, assuming no underlying mean bias in the data. The model was trained using the same 145 snapshots from the dataset to learn the correlation structure of the latent space mapping.

## Analysis of Model Performance and Computational Efficiency

### 5.1 Flow Field Reconstruction Accuracy

The ultimate test of the Reduced Order Models is their ability to accurately reconstruct the full high-fidelity flow field from a new, unseen low-fidelity input. The reconstruction process follows a four-step algorithm:

This reconstruction process follows a four-step algorithm, as detailed below.

1. **Generate a Low-Fidelity Snapshot:** For a new set of input parameters, a low-fidelity (LF) simulation is run to obtain the corresponding solution vector, or "snapshot,"  $\mathbf{x}_l$ .
2. **Project onto the Low-Fidelity Basis:** The new snapshot  $\mathbf{x}_l$  is projected onto the pre-computed LF basis,  $\Psi_l$ , to obtain its low-dimensional representation (the coefficient vector),  $\mathbf{a}_l$ .

$$\mathbf{a}_l = \Psi_l^T \mathbf{x}_l \quad (5.1)$$

3. **Map to the High-Fidelity Latent Space:** The trained surrogate model,  $f_{\text{surrogate}}$ , is used to map the low-fidelity coefficients,  $\mathbf{a}_l$ , to the predicted high-fidelity coefficients,  $\hat{\mathbf{a}}_h$ .

$$\hat{\mathbf{a}}_h = f_{\text{surrogate}}(\mathbf{a}_l) \quad (5.2)$$

4. **Reconstruct the High-Fidelity Flow Field:** The full high-fidelity flow field,  $\hat{\mathbf{x}}_h$ , is reconstructed by combining the predicted HF coefficients,  $\hat{\mathbf{a}}_h$ , with the pre-computed high-fidelity basis vectors,  $\Psi_h$ .

$$\hat{\mathbf{x}}_h \approx \Psi_h \hat{\mathbf{a}}_h \quad (5.3)$$

#### 5.1.1 Neural Network Reconstruction

The Neural Network-based ROM demonstrated high accuracy. For a representative test case with an inlet total temperature of 927 K, the reconstructed fields were qualitatively very similar to the ground truth full-order model (FOM) results, as shown in Figures 5.1–5.3. The maximum absolute relative error obtained on all test dataset occur for the wall heat flux was of only 5.97%, making most of predictions almost indistinguishable from

the high-fidelity simulation results, as shown in figure 5.4, confirming the model's ability to accurately predict the critical quantities of interest.

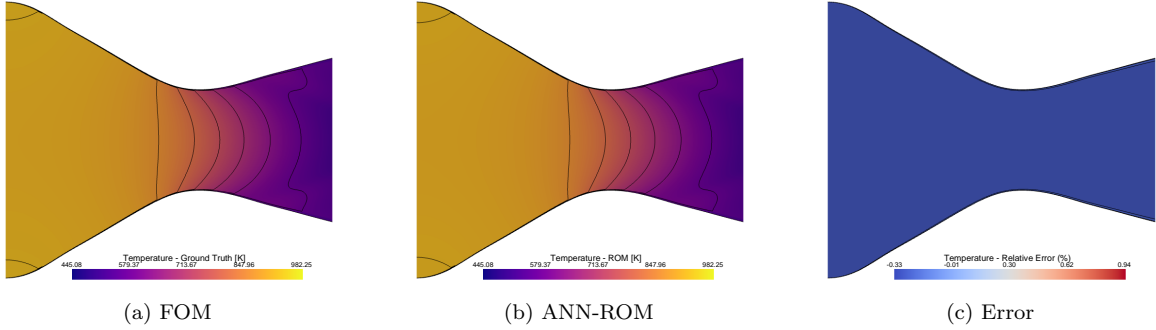


Figure 5.1: Temperature field: (a) ground truth (FOM), (b) ANN-ROM prediction, (c) absolute error.

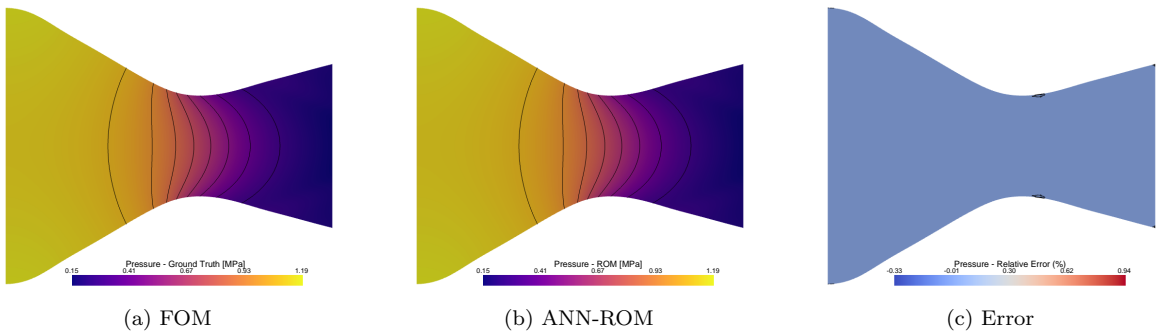


Figure 5.2: Pressure field: (a) ground truth (FOM), (b) ANN-ROM prediction, (c) absolute error.

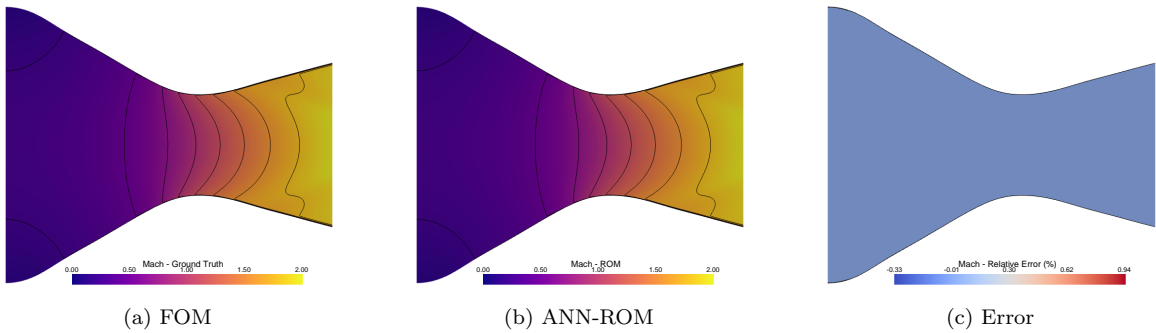


Figure 5.3: Mach number field: (a) ground truth (FOM), (b) ANN-ROM prediction, (c) absolute error.

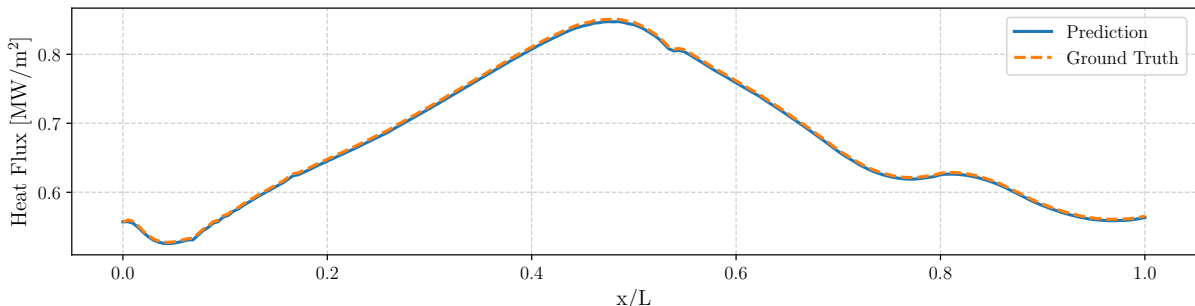


Figure 5.4: Comparison of wall heat flux between the FOM and ANN-ROM.

The Kriging-based ROM achieved even higher accuracy than the neural network approach. For the same representative test case, the reconstructed fields were visually indistinguishable from the ground truth full-order model (FOM) results, as shown in Figures 5.5–5.7. The maximum absolute relative error obtained on all test dataset also occur for the wall heat flux was of only 5.6%, slightly lower then ANN counterpart. For most of cases, the predicted wall heat flux distribution was also virtually identical to the high-fidelity simulation, confirming the Kriging model’s exceptional predictive capability as show on Figure 5.8.

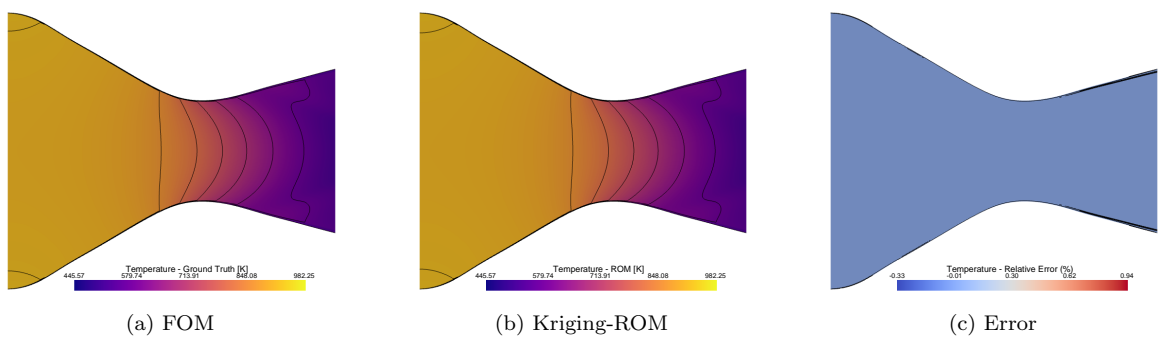


Figure 5.5: Temperature field: (a) ground truth (FOM), (b) Kriging-ROM prediction, (c) absolute error.

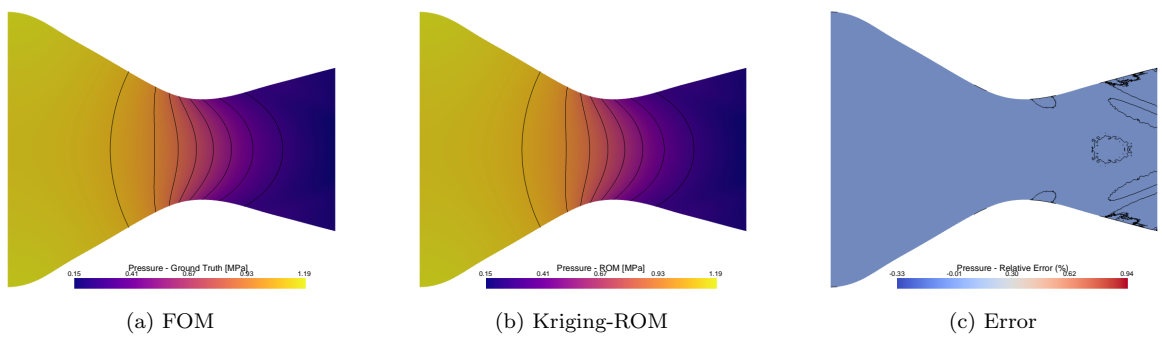


Figure 5.6: Pressure field: (a) ground truth (FOM), (b) Kriging-ROM prediction, (c) absolute error.

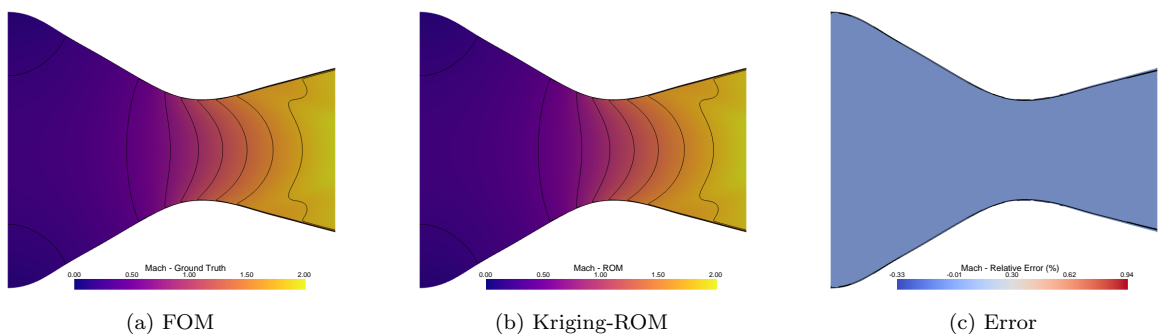


Figure 5.7: Mach number field: (a) ground truth (FOM), (b) Kriging-ROM prediction, (c) absolute error.

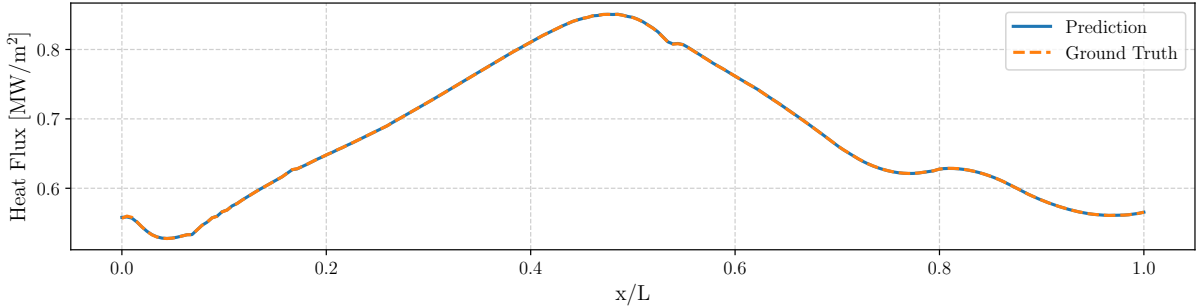


Figure 5.8: Comparison of wall heat flux between the FOM and Kriging-ROM.

## 5.2 A Comparative Assessment of Surrogate Modeling Techniques

A central contribution of this research is the direct, quantitative comparison between the modern machine learning approach (ANN) and the established statistical method (Kriging). The performance of both models, along with the baseline simulations, is synthesized in Table 5.1.

Table 5.1: Computational cost and accuracy comparison for Kriging and Neural Network (NN) metamodels. Best results are in **bold** and worst results in *italics*.

CPU time [s]	Speedup w.r.t. High-Fidelity		Pressure		Temperature		Mach		Heat Flux	
			NRMSE	MaxRelError	NRMSE	MaxRelError	NRMSE	MaxRelError	NRMSE	MaxRelError
	High-fidelity model	$1.53 \times 10^3$	-	-	-	-	-	-	-	-
Low-fidelity model	$1.02 \times 10^0$	$1.50 \times 10^3$	-	-	-	-	-	-	-	-
NN training	$3.17 \times 10^2$	-	$2.08 \times 10^{-6}$	$2.48 \times 10^{-2}$	$2.12 \times 10^{-3}$	$5.70 \times 10^{-1}$	$5.77 \times 10^{-5}$	$1.06 \times 10^0$	$1.28 \times 10^{-3}$	$5.97 \times 10^0$
Kriging training	<b><math>5.70 \times 10^0</math></b>	-	<b><math>1.89 \times 10^{-6}</math></b>	<b><math>2.43 \times 10^{-2}</math></b>	<b><math>5.50 \times 10^{-5}</math></b>	<b><math>3.95 \times 10^{-1}</math></b>	<b><math>4.24 \times 10^{-5}</math></b>	<b><math>9.96 \times 10^{-1}</math></b>	<b><math>3.07 \times 10^{-4}</math></b>	<b><math>5.60 \times 10^0</math></b>
Single NN evaluation	$2.30 \times 10^{-1}$	$6.66 \times 10^3$	-	-	-	-	-	-	-	-
Single Kriging evaluation	<b><math>4.00 \times 10^{-2}</math></b>	<b><math>3.83 \times 10^4</math></b>	-	-	-	-	-	-	-	-

The results clearly show that while both ROMs provide massive speedups, the Kriging model is superior in every metric: it is faster to train, faster to evaluate, and slightly more accurate. This counter-intuitive result, where a "classic" statistical method outperforms a more "modern" neural network, warrants deeper analysis. The reason for Kriging's superior performance likely lies in the specific nature of this engineering problem: a relatively small training dataset (145 points) is used to learn a smooth, low-dimensional mapping (10 input variables to 10 output variables). Artificial Neural Networks are highly flexible models with a large number of free parameters (weights and biases). While this flexibility is a great strength for complex, high-dimensional problems with vast amounts of data, it can be a weakness with smaller datasets, where the network may struggle to generalize perfectly. Kriging, in contrast, is a method specifically designed for interpolation from sparse data (Jones et al., 1998; Ng; Hughes, 2018). Its underlying statistical assumptions—that the function is a realization of a Gaussian process with a certain spatial correlation—provide

a strong "inductive bias". This bias constrains the model, guiding it to find the best linear unbiased predictor based on the correlations observed in the limited training data (Rasmussen; Williams, 2006; Sacks et al., 1989). For this particular problem, Kriging's statistically-grounded approach proved to be a more efficient and robust strategy for interpolation than the more flexible but less constrained neural network. This finding serves as an important reminder for the engineering community: the application of complex deep learning models is not always the optimal path, and mature statistical techniques should be carefully considered, as they may be more appropriate and effective for the problem at hand.

### **5.3 Evaluation of Computational Gains and Engineering Impact**

The practical implications of this research are profound. The Kriging-based ROM achieves a speedup of over 38,000 times compared to the high-fidelity simulation, reducing a computation that takes over 25 minutes to just 0.04 seconds, with negligible loss in accuracy (Carvalho et al., 2023). This dramatic acceleration transforms the landscape of what is possible in nozzle design and analysis.

Previously infeasible studies are now brought within reach. For instance, a comprehensive multi-objective design optimization, which might require tens of thousands of function evaluations to explore trade-offs between performance and structural integrity, can now be performed in hours instead of years (Deb et al., 2002; Toffol; Ricci, 2018). Full-scale uncertainty quantification, propagating uncertainties in manufacturing tolerances or operational conditions through the model to predict the reliability of the design, becomes a tractable problem (Le maître; Knio, 2010; Ng; Hughes, 2018). Furthermore, the near-instantaneous prediction speed opens the door to applications in inverse design (determining the nozzle shape required to produce a desired flow field) and even real-time control systems for advanced propulsion concepts (Carvalho et al., 2023; Hesthaven et al., 2016).

## Synthesis, Conclusions, and Future Directions

### 6.1 Synthesis of Findings

This dissertation has successfully detailed the development and validation of a multi-fidelity, data-driven framework capable of accelerating the aerothermodynamic analysis of convergent-divergent nozzles by orders of magnitude. The key achievements of this work can be synthesized as follows:

- A robust multi-fidelity simulation workflow was established, coupling a high-fidelity 2D RANS-CHT solver (SU2) with a computationally inexpensive quasi-1D Euler solver. Both models were rigorously verified and validated.
- Proper Orthogonal Decomposition was shown to be exceptionally effective at dimensionality reduction, compressing the high-dimensional state of the flow field into a compact latent space of only 10 variables with minimal information loss.
- Two distinct machine learning-based surrogate models—an Artificial Neural Network and a Kriging interpolator—were successfully implemented and trained to map the low-fidelity latent space to the high-fidelity latent space.
- Quantitative analysis demonstrated that the resulting Reduced Order Models can reconstruct the high-fidelity flow field and critical wall heat transfer quantities with high accuracy, achieving a computational speedup of up to 38,000 times over the full-order model.

### 6.2 Concluding Remarks

The central conclusion of this work is twofold. First, it confirms that data-driven, non-intrusive Reduced Order Models provide a powerful and effective strategy for bridging the fidelity gap in the computational analysis of complex engineering systems like rocket nozzles. They successfully leverage the speed of simple models and the accuracy of complex ones, breaking the traditional compromise between computational cost and predictive fidelity. Second, and perhaps more significantly, this study demonstrates that for engineering problems characterized by smooth, low-dimensional mappings and limited data availability, established statistical methods like Kriging can outperform more complex, modern deep

learning architectures in terms of accuracy, training cost, and evaluation speed. This highlights the critical importance of selecting a modeling technique that is appropriate for the specific structure and scale of the problem at hand.

## 6.3 Future Directions and Broader Impact

While this study has established a successful framework, several promising avenues for future research exist that could extend its capabilities and impact.

- **Geometric Variations:** The current model is parameterized only by an inlet boundary condition. A significant extension would be to incorporate variations in the nozzle geometry itself, such as the contour shape or throat radius. This would require a more sophisticated parameterization of the geometry (e.g., using B-splines or Class Shape Function Transformations) and a substantially larger training dataset to cover the expanded design space (Bekemeyer et al., 2025; Samareh, 2001).
- **Extension to 3D:** Applying this methodology to full three-dimensional nozzle simulations is the next logical step toward industrial relevance. This presents significant challenges, as the computational cost of the HF model and the sheer size of the data snapshots increase by orders of magnitude, demanding more advanced data handling and potentially more sophisticated ROM techniques (Carlberg et al., 2018).
- **Advanced ROM Techniques:** Future work could explore more advanced data-driven methods. For non-linear dimensionality reduction, deep autoencoders could be investigated as an alternative to the linear basis of POD (Erichson et al., 2020; Kutz, 2017). For unsteady flows, where transient behavior is important, methods like Dynamic Mode Decomposition (DMD) could be employed to capture the temporal dynamics of the system (Hesthaven et al., 2016; Rowley; Dawson, 2017).
- **Integration into Optimization Loops:** The validated Kriging-based ROM is an ideal candidate for integration into a formal design optimization framework. It could be coupled with a multi-objective genetic algorithm, such as NSGA-II, to perform rapid optimization of the nozzle shape or its cooling channel design to maximize performance while respecting thermal constraints (Deb et al., 2002).
- **Uncertainty Quantification:** The Kriging model's inherent ability to provide a prediction variance should be fully exploited. This would enable a comprehensive Uncertainty Quantification (UQ) analysis, allowing designers to understand how uncertainties in input parameters (e.g., material properties, operating conditions) propagate to uncertainties in key performance metrics, leading to more robust designs (Le maître; Knio, 2010; Ng; Hughes, 2018; Yu; Hesthaven, 2019).

The impact of this research contributes to the ongoing shift in engineering design towards a "digital twin" paradigm. By creating fast and accurate virtual representations of physical assets, these data-driven models enable continuous monitoring, real-time optimization, and predictive maintenance, paving the way for the next generation of intelligent and efficient aerospace systems (Glaessgen; Stargel, 2012; Rasheed et al., 2020).

## Bibliography

- ANDERSON, J. **Modern Compressible Flow**: With Historical Perspective. [S.l.]: McGraw-Hill Education, 2003. (Aeronautical and Aerospace Engineering Series).
- ARINA, R. Numerical simulation of near-critical fluids. **Applied Numerical Mathematics**, [S.l.], v.51, n.4, p.409–426, 2004.
- BACK, L.; MASSIER, P.; GIER, H. Convective heat transfer in a convergent-divergent nozzle. **International Journal of Heat and Mass Transfer**, [S.l.], v.7, p.549–568, 1964.
- BEKEMEYER, P.; HE, Q.; JAMMALAMADAKA, A.; PIAT, M.; CEZE, M.; GOMAN, O.; FARES, E. Introduction of Applied Aerodynamics Surrogate Modeling Benchmark Cases. In: AIAA SCITECH 2025 FORUM, 2025, Orlando, FL. **Anais...** AIAA, 2025.
- BENNER, P.; GUGERCIN, S.; WILLCOX, K. A Survey of Projection-Based Model Reduction Methods for Parametric Dynamical Systems. **SIAM Review**, [S.l.], v.57, n.4, p.483–531, 2015.
- BERKOOZ, G.; HOLMES, P.; LUMLEY, J. L. The proper orthogonal decomposition in the analysis of turbulent flows. **Annual Review of Fluid Mechanics**, [S.l.], v.25, n.1, p.539–575, 1993.
- BRUNTON, S.; KUTZ, J. **Data-driven science and engineering**. Cambridge, England: Cambridge University Press (Virtual Publishing), 2019.
- CARLBERG, K.; BRENCHER, L.; BENNER, P. Model reduction for large-scale systems with applications in computational fluid dynamics. In: **Model Reduction of Complex Dynamical Systems**. [S.l.]: Springer, 2018. p.31–60.
- CARVALHO, A. M.; DEZAN, D.; FERREIRA, W. Data-driven flow reconstruction using low fidelity simulation for compressible flow predictions in convergent-divergent nozzles. In: ABCM INTERNATIONAL CONGRESS OF MECHANICAL ENGINEERING (COBEM 2023), 27., 2023. **Proceedings...** [S.l.: s.n.], 2023.

- DEB, K.; PRATAP, A.; AGARWAL, S.; MEYARIVAN, T. A. M. T. A fast and elitist multiobjective genetic algorithm: NSGA-II. **IEEE Transactions on Evolutionary Computation**, [S.l.], v.6, n.2, p.182–197, 2002.
- ECONOMON, T.; PALACIOS, F.; COPELAND, S.; LUKACZYK, T.; ALONSO, J. SU2: An open-source suite for multiphysics simulation and design. **AIAA Journal**, [S.l.], v.54, n.3, p.828–846, 2016.
- ERICHSON, N.; MATHELIN, L.; YAO, Z.; BRUNTON, S.; MAHONEY, M.; KUTZ, J. Shallow neural networks for fluid flow reconstruction with limited sensors. **Proceedings of the Royal Society A: Mathematical, Physical and Engineering Sciences**, [S.l.], v.476, n.2238, p.20200097, 2020.
- FORRESTER, A.; SÓBESTER, A.; KEANE, A. **Engineering Design via Surrogate Modelling**. [S.l.]: Wiley, 2008.
- GLAESGEN, E.; STARGEL, D. The digital twin paradigm for future NASA and US Air Force vehicles. In: AIAA/ASME/ASCE/AHS/ASC STRUCTURES, STRUCTURAL DYNAMICS AND MATERIALS CONFERENCE 20TH AIAA/ASME/AHS ADAPTIVE STRUCTURES CONFERENCE 14TH AIAA, 53., 2012. **Anais...** [S.l.: s.n.], 2012. p.1818.
- HESTHAVEN, J.; ROZZA, G.; STAMM, B. **Certified Reduced Basis Methods for Parametrized Partial Differential Equations**. [S.l.]: Springer International Publishing, 2016.
- HIRSCH, C. **Numerical Computation of Internal and External Flows. Volume 1: Fundamentals of Numerical Discretization**. [S.l.]: John Wiley & Sons, Inc., 1988.
- HIRSCH, C. **Numerical Computation of Internal and External Flows, Volume 2: Computational Methods for Inviscid and Viscous Flows**. Chichester: John Wiley & Sons, 1990. 691p.
- HOLMES, P.; LUMLEY, J. L.; BERKOOZ, G. **Turbulence, Coherent Structures, Dynamical Systems and Symmetry**. [S.l.]: Cambridge University Press, 2012.
- HORNIK, K.; STINCHCOMBE, M.; WHITE, H. Multilayer feedforward networks are universal approximators. **Neural Networks**, [S.l.], v.2, n.5, p.359–366, 1989.
- JONES, D. R.; SCHONLAU, M.; WELCH, W. J. Efficient global optimization of expensive black-box functions. **Journal of Global Optimization**, [S.l.], v.13, n.4, p.455–492, 1998.
- KUTZ, J. N. Deep learning in fluid dynamics. **Journal of Fluid Mechanics**, [S.l.], v.814, p.1–4, 2017.

LE MAÎTRE, O.; KNIO, O. M. **Spectral Methods for Uncertainty Quantification:** With Applications to Computational Fluid Dynamics. [S.l.]: Springer Science & Business Media, 2010.

MENTER, F. R. Two-equation eddy-viscosity turbulence models for engineering applications. **AIAA Journal**, [S.l.], v.32, n.8, p.1598–1605, 1994.

NG, F.; HUGHES, A. Reconstructing ice-flow fields from streamlined subglacial bedforms: A kriging approach. **Earth Surface Processes and Landforms**, [S.l.], v.44, n.4, p.861–876, 2018.

PALACIOS, F. et al. SU2: An open-source suite for multiphysics simulation and design, version 7. **AIAA Journal**, [S.l.], 2022.

QUARTERONI, A.; MANZONI, A.; NEGRI, F. **Reduced Basis Methods for Partial Differential Equations:** An Introduction. [S.l.]: Springer International Publishing, 2016. (UNITEXT, v.92).

RASHEED, A.; SAN, O.; KVAMSDAL, T. Digital twin: Roles, challenges and opportunities. **arXiv preprint arXiv:2001.07135**, [S.l.], 2020.

RASMUSSEN, C. E.; WILLIAMS, C. K. I. **Gaussian Processes for Machine Learning.** [S.l.]: MIT Press, 2006.

ROWLEY, C. W.; DAWSON, S. T. M. Model Reduction for Flow Analysis and Control. **Annual Review of Fluid Mechanics**, [S.l.], v.49, p.387–417, 2017.

SACKS, J.; WELCH, W. J.; MITCHELL, T. J.; WYNN, H. P. Design and analysis of computer experiments. **Statistical Science**, [S.l.], v.4, n.4, p.409–423, 1989.

SAMAREH, J. A. Survey of shape parameterization techniques for high-fidelity multidisciplinary design optimization. **AIAA Paper**, [S.l.], v.1, p.1–13, 2001.

SIROVICH, L. Turbulence and the dynamics of coherent structures. Part 1: Coherent structures. **Quarterly of Applied Mathematics**, [S.l.], v.45, n.3, p.561–571, 1987.

STABILE, G.; ROZZA, G. Reduced Order Models for Computational Fluid Dynamics. **Fluids**, [S.l.], v.6, n.1, p.1, 2021.

SU2 Development Team. **Governing Equations in SU2**. Acessado em 12 de agosto de 2025, [https://su2code.github.io/docs\\_v7/Theory/](https://su2code.github.io/docs_v7/Theory/).

SUTTON, G.; BIBLARZ, O. **Rocket Propulsion Elements.** [S.l.]: John Wiley & Sons, 2010.

- TAIRA, K.; BRUNTON, S. L.; DAWSON, S. T. M.; ROWLEY, C. W.; COLONIUS, T.; MCKEON, B. J. et al. Modal analysis of fluid flows: An overview. **AIAA Journal**, [S.l.], v.55, n.12, p.4013–4041, 2017.
- TOFFOL, F.; RICCI, S. A methodology for the structural optimization of a transport aircraft wing box including aeroelastic constraints. **Aerospace Science and Technology**, [S.l.], v.78, p.473–487, 2018.
- ENGBLOM, W.; FLETCHER, B.; GEORGIADIS, N. **Validation of Conjugate Heat-Transfer Capability for Water-Cooled High-Speed Flows**. [S.l.: s.n.].
- VERSTEEG, H.; MALALASEKERA, W. **An Introduction to Computational Fluid Dynamics**: The Finite Volume Method. [S.l.]: Pearson Education Limited, 2007.
- WHITE, F. **Fluid Mechanics**. [S.l.]: McGraw Hill, 2011. (McGraw-Hill series in mechanical engineering).
- WILCOX, D. C. **Turbulence Modeling for CFD**. [S.l.]: DCW Industries, 1998.
- YU, J.; HESTHAVEN, J. Flowfield reconstruction method using artificial neural network. **AIAA Journal**, [S.l.], v.57, n.2, p.482–498, 2019.
- ZUCROW, M.; HOFFMAN, J. **Gas Dynamics, Volume 1**. [S.l.]: Wiley, 1976. n.v. 1. (Gas Dynamics).